学位論文

デュアル光コム屈折率センシングと

バイオセンシング応用に関する研究

2024 年 9 月

宮村　祥吾

PhD thesis

Study on dual-comb refractive index sensing and its applications in biosensing

September 2024

Shogo Miyamura

Index

1. Introduction

Refractive index (RI) is defined as the ratio of the speed of light in a vacuum to the speed of light propagating through a substance. Light propagating through a substance interacts with the atoms in the substance, and by precisely measuring the RI, the properties of the substance can be deciphered. In practice, RI measurements are applied in various fields such as quality control in food, pharmaceuticals, and chemical industrial products, characterization of optical components, and virus antigen testing.

Several methods have been proposed for RI measurements. For instance, the minimum deviation method [1] involves directing light onto a sample processed into a prism shape and measuring the angle of deviation of the transmitted light. The RI resolution is approximately ~1×10^{-5}. The critical angle method [1] measures the angle (critical angle) at which total reflection light occurs at the boundary surface between a prism and a sample. The RI resolution is approximately ~1×10^{-4}. The V-block method [1] involves placing a sample on a V-block prism, directing light onto the prism's wall surface normal, and measuring the angle of light refracted by the prism and sample from the prism's wall surface. The RI resolution is approximately ~2×10^{-5}. The surface plasmon resonance (SPR) method [2] measures the spectrum or angle shift of the SPR dip on a gold thin film deposited on a prism. The RI resolution is approximately ~1×10^{-5}. These conventional methods measure changes in intensity at specific wavelengths or shifts in peak wavelength, but all are limited to RI resolutions of approximately 10^{-4} to 10^{-5} due to the performance of the measuring equipment. In the industrial sector, further high-precision and high-resolution RI measurements are required to conduct higher-quality inspections. Versatility and practicality are also considered significantly important.

RI sensors based on optical fibers are considered powerful tools that meet the requirements for RI measurements mentioned above. Optical fiber RI sensors offer compactness, flexibility, immunity to electrical noise, and explosion-proof characteristics, enabling their use in various environments. Indeed, examples of their applications include concentration measurements of sucrose [3], gas pressure measurements [4], and biomolecule measurements [5]. Conventional optical fiber RI sensors include optical fiber SPR sensors [6], fiber Bragg grating [7], and multi-mode interference (MMI) sensors [8], all of which detect RI changes by converting them into shifts in optical wavelength. However, these conventional optical fiber RI sensors were limited in RI measurement resolution by the constraints of the width of the optical spectrum or the resolution of the optical spectrum analyzer. If RI changes could be converted into photonic RF signals (a few MHz ~ several tens MHz), RI sensors signal could be electrically detected, enabling measurement with inexpensive and simplified configurations. Moreover, higher measurement accuracy is guaranteed by comparison with electric frequency standards. RF-readout fiber sensors

have been used in strain sensors [9] and ultrasonic sensors [10,11] by measuring laser multi-longitudinal modes or multi-polarization modes in CW laser, but the inherent frequency fluctuations between modes limited the accuracy of RI measurements.

Recently, optical frequency combs (OFC) [12-14] have been proposed as mechanisms for converting from optical frequency signal to photonic RF signal. When OFC are observed in the optical frequency domain, they exhibit a discrete spectrum of longitudinal mode columns arranged at equal intervals like the teeth of a comb. Since all longitudinal modes are traceable to frequency standards via laser control, OFC can be used as a precise ruler for optical frequencies. Based on the concept of optical frequency rulers, OFC have been used in frequency and distance measurements. For example, they have been applied in atomic spectroscopic [13], gas spectroscopy [15], spectroscopic ellipsometry [16], strain sensors [17], and distance measurements [18].

When OFC are observed in the time domain, they exhibit a series of ultra-short pulses. Each longitudinal mode on the optical frequency axis has coherence, and interference occurs between modes by synchronizing phases (mode-locking), forming periodic reinforcing interference in the time domain to generate a series of ultra-short pulses. The repetition frequency of the series of ultra-short pulses in the time domain is equal to the interval between each longitudinal mode in the optical frequency domain, and is always constant for all longitudinal modes. This repetition frequency f_{rep} is given by

$$f_{rep} = \frac{c}{nL} \tag{1}$$

where c is the speed of light in a vacuum, n is the refractive index of the resonator, and L is the resonator length. Thus, the f_{rep} can be set to any value by adjusting the refractive index and geometrical length in the cavity. Additionally, to determine the absolute frequency in the optical frequency domain, it is necessary to define an offset component f_{ceo} that occurs when extending the longitudinal modes to the origin of the optical frequency axis at f_{rep} intervals. The absolute frequency f_m of the m-th longitudinal mode is obtained by

$$f_m = mf_{rep} + f_{ceo} \tag{2}$$

The above equations show the close relationship between the optical frequency f_m of the OFC and the RF frequency f_{rep}, indicating the basis for the conversion of optical-to-RF frequencies by OFC. As mentioned earlier, measurements in the RF domain offer advantages of high precision, high functionality, high convenience, and low cost, and RF signals and their harmonics have been applied to highly accurate long-distance measurements [19-21].

Recently, fiber OFC, composed of optical fibers, have been applied to various applications such as strain sensing [22], acoustic sensing [23], and ultrasonic sensing [24]. This is enabled by

the function of converting disturbances acting on the cavity into RF frequencies. When disturbances such as vibrations act on the cavity of the fiber OFC, the optical path length nL in Eq. (1) changes, resulting in a change in f_{rep}. In other words, the fiber OFC can convert disturbances acting on the optical fibers of the cavity into changes in RF frequency. RF frequency measurement allows for a wide dynamic range and high-precision measurement using electric frequency standards. By combining fiber OFCs with sensors that convert disturbances into RF frequencies, it is possible to realize photonic RF sensors that significantly improve accuracy and dynamic range compared to conventional electrical or optical measurement methods. However, when using a single-mode fiber within the cavity as a sensor, there is a challenge that measurement is limited to physical quantities directly affecting the resonator, such as strain [22], sound [23], or ultrasound [24].

By inserting a fiber sensor sensitive to specific physical quantities into the cavity, it is possible to create an photonic RF sensor capable of sensing those physical quantities. One interesting application of photonic RF sensors is RI measurements, where transitioning from conventional optical spectrum measurement methods to RF frequency measurement methods significantly improves sensing accuracy. One technique for performing RI measurements using photonic RF sensors involves combining fiber OFC with MMI fiber sensors [25-27]. An MMI fiber sensor consists of a clad-less multi-mode fiber (MMF) with a pair of single-mode fibers (SMFs) at both ends, and it can be seamlessly connected to fiber OFC via fusion splicing. When an MMI fiber sensor is immersed in a sample solution, a Goos-Hänchen shift dependent on the RI of the solution sample occurs at the interface of the clad-less MMF, causing a wavelength λ_{MMI} propagating inside the resonator to shift. This shift in λ_{MMI} induces a change in n in Eq. (1) due to the cavity's wavelength dispersion, ultimately converting the refractive index change into a shift in RF frequency. RI measurements of ethanol-water solutions using this method have achieved a refractive index resolution of 4.88×10^{-6}, demonstrating higher accuracy than conventional RI measurement methods [28]. However, this method faces challenges due to temperature drift affecting RF frequency fluctuations within the cavity [29], particularly in measuring RI changes for samples with small refractive index variations, such as biosamples.

Therefore, we investigated a new temperature compensation method for RI-sensing OFC and developed dual-comb RI-sensing incorporating temperature compensation based on the active-dummy method. To evaluate the temperature compensation performance of dual-comb RI-sensing, we investigated the influence of temperature drift on the difference in cavity lengths between the active-sensing OFC and the dummy-sensing OFC. Additionally, considering the fiber processing accuracy of the fiber cavity, we also examined how much error in cavity length difference can be tolerated. We also discussed other elements besides the cavity length difference

that contribute to reducing temperature drift. Furthermore, we expanded dual-comb RI-sensing to biosensing based on antigen-antibody reactions, which were difficult to measure due to temperature drift effects in conventional RI-sensing OFC, and conducted its characterization evaluation.

This doctoral dissertation is structured around two main themes:

(1) Reduction of temperature drift in refractive-index-sensing optical frequency comb by active-dummy compensation of dual-comb configuration [78]

(2) Rapid, high-sensitivity detection of biomolecules using dual-comb biosensing [79]

In the first theme, we investigated a new temperature compensation method for RI-sensing optical combs. We focused on the active-dummy compensation method used in strain sensors. This method involves obtaining the differential signal between an active gauge measuring both temperature and strain and a dummy gauge measuring only temperature, thereby compensating for environmental temperature disturbances and extracting strain measurements. We extended this principle to RI-sensing OFC, enabling temperature-compensated RI-sensing OFCs (dual-comb RI-sensing). To evaluate the temperature compensation performance of dual-comb RI-sensing, we investigated the impact of temperature drift on the difference in cavity lengths between the active-sensing and dummy-sensing OFCs. While ideally the cavity lengths of the active-sensing and dummy-sensing OFCs should be exactly the same, considering the fiber processing precision of the resonators, we also discussed the acceptable level of error. We also explored other factors besides resonator length difference that could contribute to reducing temperature drift.

In the second theme, we applied dual-comb RI-sensing to biosensing. By modifying SARS-CoV-2 N protein antibodies on an MMI fiber sensor surface, we measured the concentration changes of antigens as changes in RF frequency. We conducted a quantitative analysis of the sensing performance and compared it with other methods of SARS-CoV-2 testing to confirm the advantages and challenges of this approach.

2. Reduction of temperature drift in refractive-index-sensing optical frequency comb by active-dummy compensation of dual-comb configuration

2.1 Introduction

Optical fiber sensor [67,68]has been often used for refractive-index (RI) sensing and RI-sensing-based applications[69-73]. RI fiber sensor benefits from inherent advantages of fiber sensor such as lightweight, small size, flexibility, cost effectiveness, immunity to electromagnetic interference, and environmental ruggedness. Various types of RI fiber sensors have been developed: tapered fiber [74], core-offset fiber [75], fiber Bragg grating (FBG) [76], surface plasmon resonance (SPR) [77], and multimode interference (MMI) [8]. Most of RI fiber sensors measures RI-dependent shift of optical spectrum peak or dip. However, the small shift to the relatively broad bandwidth in a spectral peak or dip as well as a limited spectrometer resolution often spoils the precision of those RI fiber sensors.

One potential approach to avoid the drawback of optical spectrum measurement in RI sensing is conversion of optical spectral sensor signal to photonic radio-frequency (RF) spectral sensor signal such as optical beat signal; namely, photonic RF conversion. The photonic RF conversion enables us to measure a sample RI as RF frequency signal, benefiting from high precision, wide dynamic range, convenience, and low cost in well-established electrical frequency measurements. One promising approach for photonic RF conversion is use of optical frequency comb (OFC) [12,14] because OFC has a coherent link between optical frequency of OFC line (n_m; typically, 194 THz in fiber OFC) and radio frequency of OFC line spacing (f_{rep}; typically, 100 MHz in fiber OFC) given by

$$\nu_m = f_{ceo} + mf_{rep} \tag{1}$$

where f_{ceo} is a carrier-envelope-offset frequency and m is a line number. Equation (1) indicates that an optical frequency signal of THz order can be uniquely converted to an electrical frequency signal of MHz order. Recently, fiber-OFC-based photonic RF conversion was adopted for fiber sensing of sample RI [28-30]. A fiber OFC including an intracavity MMI fiber sensor has been used for a photonic RF conversion of a sample RI into f_{rep} via a combination of RI-dependent tunable bandpass filtering by the intracavity MMI fiber sensor and the wavelength dispersion by the OFC cavity fiber. Such RI-sensing OFC enables f_{rep}-reading RI sensing; due to the ultranarrow linewidth in the mode-locking oscillation, the f_{rep} signal with the spectral linewidth below 1 Hz was precisely measured by a RF frequency counter synchronized with a rubidium frequency standard. Furthermore, the intracavity fiber sensor enables multiple interactions between the sample and the light, enhancing the sensitivity. However, the temperature drift of f_{rep} caused by the temperature fluctuation of an optical cavity length (nL) spoils the reproducibility of f_{rep}-reading RI sensing because f_{rep} in the RI-sensing OFC is free-running operation in contrast to

actively stabilized operation of usual OFCs. Because of lack of one-to-one correspondence between f_{rep} and sample RI, f_{rep} change (Δf_{rep}) measurement was performed to obtain RI change. However, such relative measurement of f_{rep} is not realistic in practical applications of RI sensing. If cavity-temperature-dependent slow drift of f_{rep} is suppressed, the absolute measurement of the sample RI will be achieved based on the one-to-one correspondence between f_{rep} and sample RI.

Recently, the active-dummy temperature-drift compensation with a dual-comb configuration was adopted for RI-sensing OFC and its application for biosensing [79]. A pair of RI-sensing OFCs was used for an active-sensing OFC and a dummy-sensing OFC. Since the active-sensing OFC provides the sensor signal (f_{rep1}) reflecting both the sample RI and the cavity temperature whereas the dummy-sensing OFC gives the sensor signal (f_{rep2}) reflecting only the cavity temperature, difference of sensor signals between them (Δf_{rep}) cancels the influence of temperature. In other words, it gives the temperature-independent sensor signal of sample RI. This dual-comb RI sensing enables the small change in the sensor signal caused by sample RI to be extracted from the large, variable background signal caused by temperature disturbance. Furthermore, it was effectively applied for rapid biosensing of severe acute respiratory syndrome coronavirus 2 (SARS-CoV-2) by help of antigen–antibody interactions. However, an investigation regarding the optimal Δf_{rep} in the context of the active-dummy temperature compensation and the one-to-one correspondence between sensor signal of Δf_{rep} and sample RI has not yet been conducted.

In this chapter, we investigate the Δf_{rep} dependence of the active-dummy temperature compensation, and then the Δf_{rep} dependence of the one-to-one correspondence between sensor signals and sample RI by using as an ethanol water solution with different RIs as a sample.

2.2 Principle of operation

Figure 2.1 shows the principle of operation for RI-sensing OFC. Since its detailed principle is given elsewhere [28-30], we briefly described it. The first key element is an intracavity MMI fiber sensor, functioning as an RI-dependent tunable optical bandpass filter inside the cavity. This leads to RI-dependent optical spectrum shift of RI-sensing OFC (center wavelength = λ_{MMI}). The second key element is wavelength dispersion of refractive index in the OFC cavity fiber, converting RI-dependent λ_{MMI} shift into RI-dependent shift of the optical cavity length nL. A relation between nL and f_{rep} is given by

$$f_{rep} = \frac{c}{nL} \tag{2}$$

where c is a velocity of light in vacuum, n and L are respectively a group refractive index and a geometrical length of fiber OFC cavity. Since f_{rep} is a function of nL, RI-dependent nL shift is equivalent to RI-dependent f_{rep} shift. Finally, one can read a sample RI as RI-dependent f_{rep}.

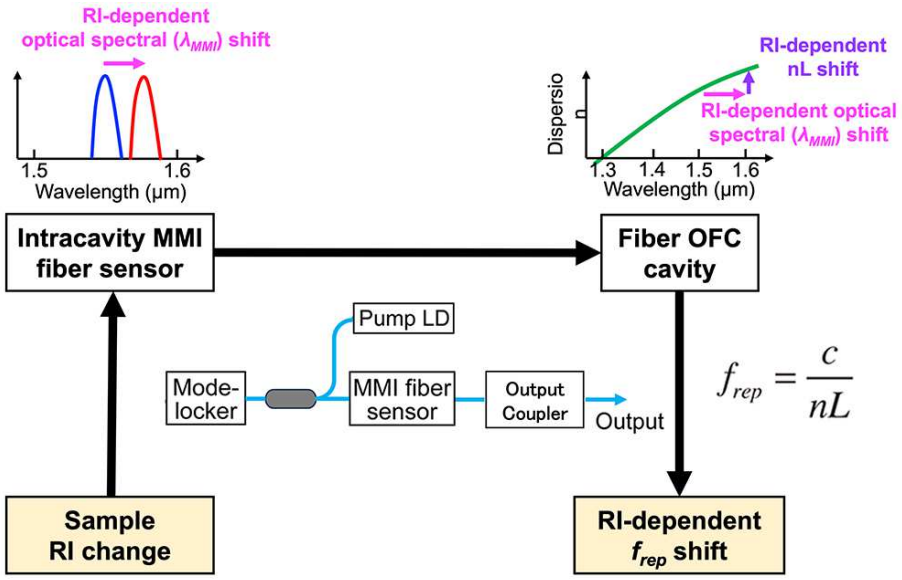

Fig. 2.1. Principle of operation for RI sensing OFC.

We next describe how to compensate the cavity-temperature-dependent drift of f_{rep} in RI-sensing OFC. We here set a pair of RI-sensing OFCs with a sample and a reference material under equivalent environmental temperature disturbance as shown in Fig. 2.2(a). When the sample RI increases stepwise while the cavity temperature changes monotonously, the sensor signal f_{rep1} of the active-sensing OFC changes depending on both sample RI and cavity temperature [blue plot in Fig. 2.2(b)]. On the other hand, when the cavity temperature change monotonously without the change of reference material RI in the dummy-sensing OFC, the sensor signal f_{rep2} of the dummy-sensing OFC reflects only the cavity temperature. Therefore, a difference between f_{rep1} and f_{rep2} ($= \Delta f_{rep} = f_{rep1} - f_{rep2}$) reflects the sample RI signal without the influence of cavity temperature change [Fig. 2.2(c)].

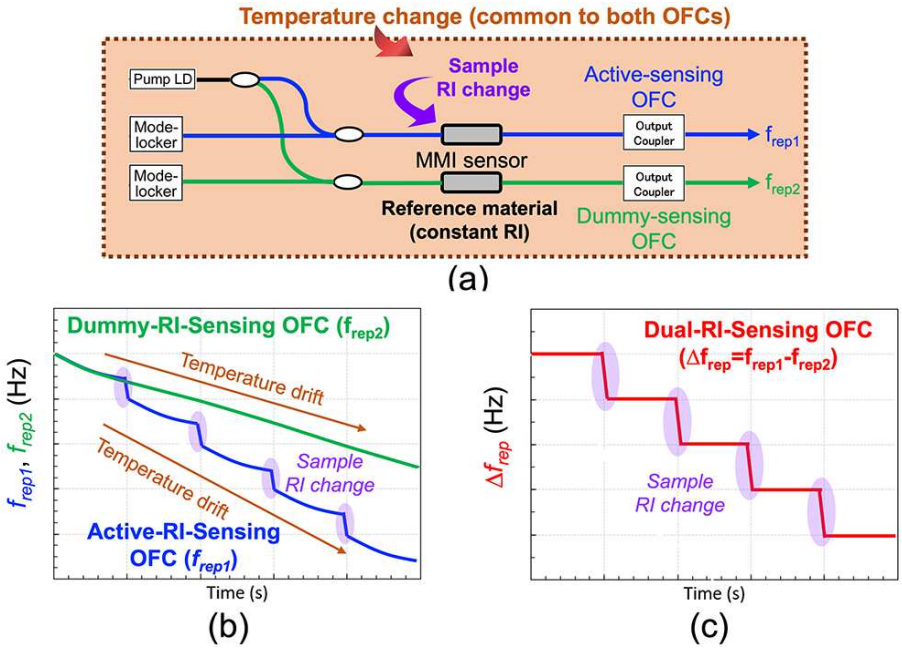

Fig. 2.2. Principle of operation for active-dummy temperature-drift compensation with dual-comb configuration in PR-sensing OFC. (a) Schematic drawing of dual-comb RI sensing setup. (b) Behavior of f_{rep1} in active-sensing OFC and f_{rep2} in dummy-sensing OFC. (c) Behavior of Δf_{rep1} in dual-comb RI sensing.

2.3 Experimental setup

Figure 2.3 shows the schematic drawing of the dual-comb RI sensing. They are based on a linear fiber cavity mode-locked by saturable absorption. Each linear cavity includes a polarization-maintaining single-mode fiber (PMF, Corning Panda PM1550, Corning, dispersion at 1550 nm = 17 ps•km^{-1}•nm^{-1}), an erbium-doped polarization-maintaining single-mode fiber (EDF, PM-ESF-7/125, Coherent, dispersion at 1550 nm = 16 ps•km^{-1}•nm^{-1}), a fiber-coupled saturable absorbed mirror (SAM-1550-55-2ps-1.3b-0, BATOP, high reflection band = 1480-1640 nm, absorbance = 55 %, modulation depth = 34 %, relaxation time constant ~ 2 ps, size = 1.3-mm width, 1.3-mm height, 0.4-mm thickness), a wavelength-division-multiplexing coupler (WDM, PMWDM-1-9801550-2-B-Q-6, AFR), a pumping laser diode (LD, BL976-PAG700, Thorlabs, wavelength = 976 nm, power = 700 mW), a 90:10 fiber-partial reflector (FPR, PMOFM-55-2-B-Q-F-90),and an intracavity MMI fiber sensor (MMI). The intracavity MMI fiber sensor was composed of a clad-less MMF (FG125LA, Thorlabs, core diameter= 125 μm, fiber length = 58. 94mm) with a pair of PMFs at both ends (core diameter=8.5μm, clad diameter=125μm, fiber length = 200 mm). Here, we set λ_{MMI} to 1556.6 nm. The fiber cavity was enclosed in a plastic box, and its temperature was controlled to 21.5 °C by a combination of a Peltier heater (TEC1-12708,

Kaito Denshi, power = 76 W), a thermistor (NXFT15WF104FA2B050, Murata), and a temperature controller (TED200, Thorlabs, PID control) (not shown in Fig. 2.3). We fixed f_{rep2} of the dummy-sensing OFC to be 31,451,121 Hz. Then, we adjusted f_{rep1} of the active-sensing OFC around 31 MHz to change Δf_{rep} within a range of a few kHz to 1,000 kHz by adjusting its cavity fiber length of the active-sensing OFC. We adopted mechanically sharing of linear fiber cavities to implement equivalent environmental temperature disturbance to the active-sensing and the dummy-sensing OFCs [31,32]. The output light from them was detected by a pair of photodetectors (PD), and f_{rep1} and f_{rep2} were measured by an RF frequency counter (53220A, Keysight Technologies, frequency resolution = 12 digit•s^{-1}) synchronized to a rubidium frequency standard (FS725, Stanford Research Systems, accuracy = 5×10^{-11} and instability = 2×10^{-11} at 1s). Additionally, its optical spectrum was measured by an optical spectrum analyzer (AQ6315A, Yokogawa Electric Corp., wavelength accuracy = 0.02 nm, wavelength resolution = 0.02 nm).

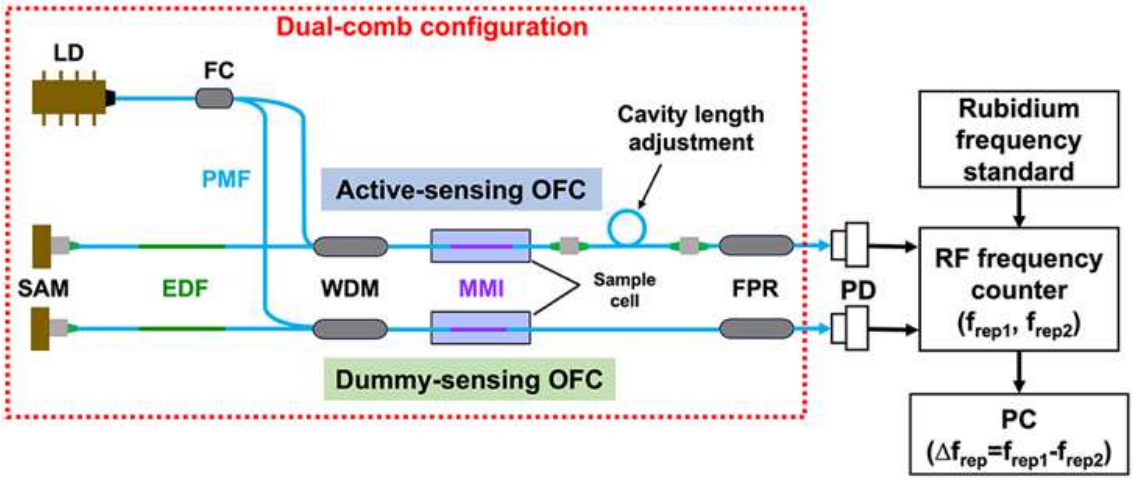

Fig. 2.3. Schematic drawing of experimental setup. LD, pumping laser diode; FC, 50:50 fiber coupler; PMF, polarization-maintaining single-mode fiber; EDF, erbium-doped polarization-maintaining single-mode fiber; SAM, fiber-coupled saturable absorbed mirror; WDM, wavelength-division-multiplexing coupler; MMI, intracavity multimode-interference fiber sensor; FPR, 90:10 fiber-partial reflector.

2.4 Results

2.4.1 Basic performance

We first evaluated basic performance of active-sensing OFC and dummy-sensing OFC when a pure water was used as a sample for them. We prepared active-sensing OFCs with different Δf_{rep} values (= 3 kHz, 46 kHz, 111 kHz, and 1,000 kHz). Figure 2.4(a) compares optical spectra of active-sensing OFC among different Δf_{rep} values (resolution bandwidth = 0.1 nm). Each

individual optical spectrum closely matches around the wavelength of 1559nm. For comparison, the optical spectrum of the dummy-sensing OFC was also measured as indicated by a black plot in Fig. 2.4(a). The overlap of optical spectra between the active-sensing OFC and the dummy-sensing OFC was not significant. The difference in overlap between them is due to the uncertainty in the clad-less MMF length of the MMI fiber sensor and hence l_{MMI}, which is caused by the fiber processing accuracy. Figures 2.4(b) and 2.4 (c) show RF spectra of active-sensing OFC with f_{rep1} and dummy-sensing OFC with f_{rep2} when Δf_{rep} was set to be 3 kHz (resolution bandwidth = 10 Hz). Similar RF spectra were observed for the active-sensing OFC with different Δf_{rep} values (not shown). The narrow linewidth characteristics enable high precision of RI sensing, but they also make the system more susceptible to environmental temperature drift effects.

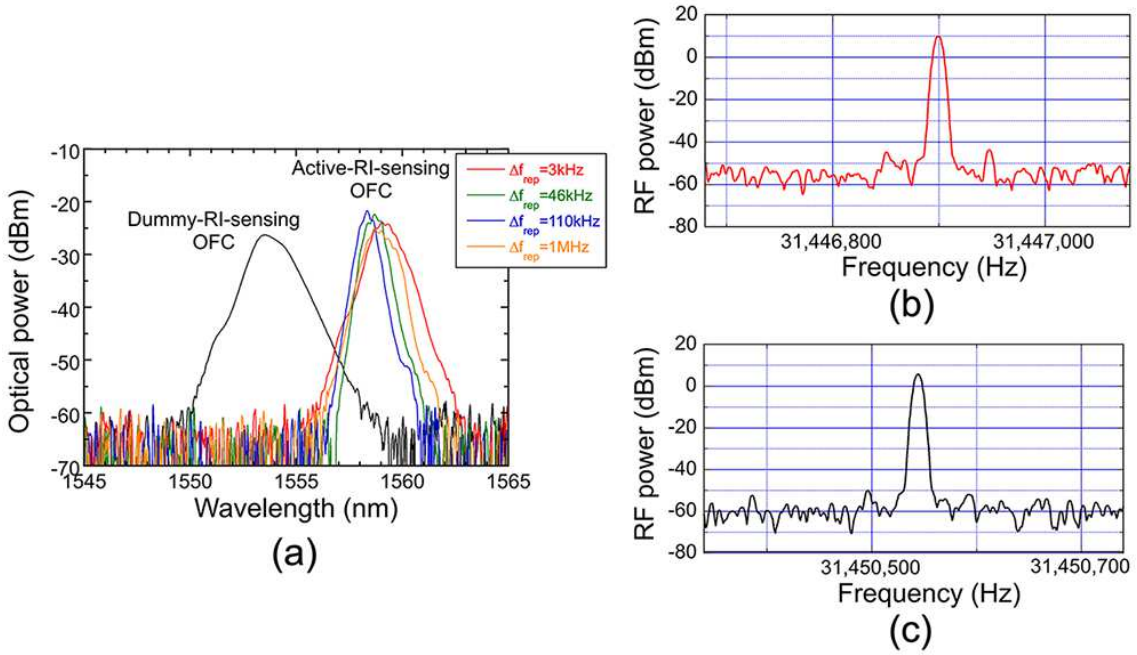

Fig. 2.4. Basic performance of active-sensing and dummy-sensing OFCs. (a) Comparison of optical spectrum between active-sensing OFC with different Δf_{rep} values and dummy-sensing OFC (RBW = 0.1 nm). RF spectra of (b) f_{rep1} and (c) f_{rep2} when Δf_{rep} = 3 kHz (RBW = 10Hz).

We next evaluated the frequency instability of f_{rep1} and f_{rep2}. Figure 2.5(a) shows a comparison of the frequency fluctuation between f_{rep1} (red plots) and f_{rep2} (black plots) with respect to gate time when Δf_{rep} was set to be 3 kHz. Since both active-sensing OFC and dummy-sensing OFC have similar cavity configuration and environment, they show similar frequency instability of f_{rep1} and f_{rep2}. A similar trend was observed for different Δf_{rep} values (not shown), confirming that the frequency fluctuations of f_{rep1} and f_{rep2} are not dependent on Δf_{rep}. We also investigated the long-term frequency variations of f_{rep1} in the active-sensing OFC. Figure 2.5(b) shows the

temporal variations of f_{rep1} within a range of 10 hours. We here defined the frequency deviation of f_{rep1} from its initial value of measurement start as δf_{rep1}. Due to changes in the optical cavity length caused by variations in ambient temperature, fluctuations of f_{rep1} within the 100 Hz range can be observed. The unidirectional increase in f_{rep1} reflects gradual changes in the cavity environment temperature, likely due to ambient temperature variations. In contrast, the periodic repetitive changes correspond to room temperature fluctuations caused by air conditioning.

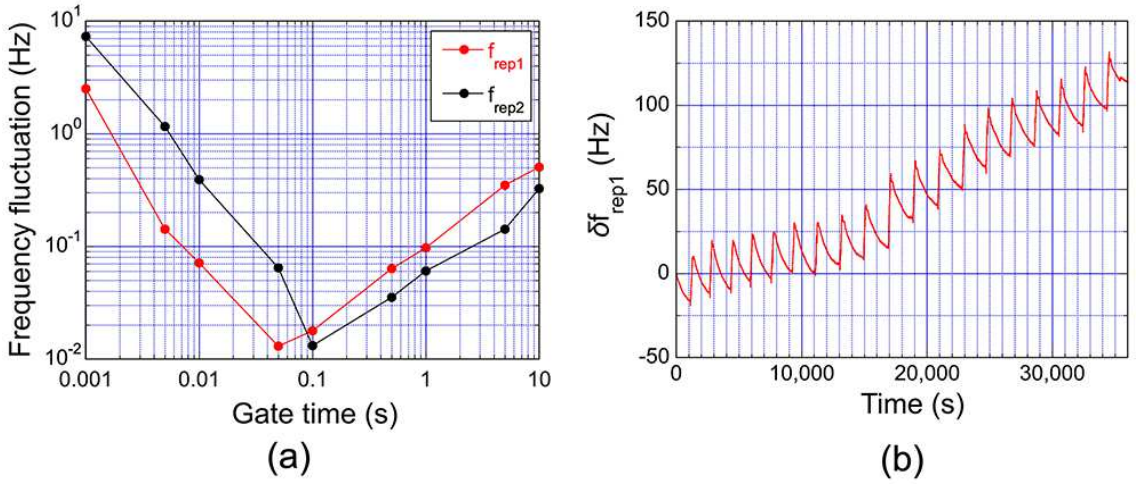

Fig. 2.5. Frequency characteristics of active-sensing and dummy-sensing OFCs. (a) Frequency fluctuation of f_{rep1} and f_{rep2} with respect to gate time. (b) Temporal variation of f_{rep1} and f_{rep2} in long term.

2.4.2 Dependence of active-dummy temperature compensation on Δf_{rep}

As shown in Fig. 2.5, the active-sensing OFC and the dummy-sensing OFC exhibited similar behaviors in frequency characteristics, which enables compensation for the temperature drift effect by taking the difference between them. Of particular interest here is how this compensation effect depends on Δf_{rep} and whether an optimal Δf_{rep} exists. Therefore, an investigation was conducted regarding the dependence of active-dummy temperature compensation on Δf_{rep} (= 3 kHz, 46 kHz, 111 kHz, and 1,000 kHz). Here, considering the results indicating changes of approximately 100Hz in f_{rep1} due to room temperature variations as shown in Fig. 2.5(b), we measured Δf_{rep} when f_{rep1} was changed by approximately 100 Hz by rapid air conditioning. We used a pure water as a sample with a constant RI for them, again. We measured the temporal variations of f_{rep1}, f_{rep2}, and Δf_{rep} when pure water was used as a sample for both OFCs. Figure 2.6 shows the temporal shifts in f_{rep1}, f_{rep2}, and Δf_{rep}, namely, δf_{rep1}, δf_{rep2}, and $\delta\Delta f_{rep}$, respectively, when Δf_{rep} was set to be (a) 3 kHz, (b) 46 kHz, (c) 111 kHz, and (d) 1000 kHz. Comparing with δf_{rep1} and δf_{rep2}, it is evident that the width of the frequency fluctuations in Δf_{rep}

has been significantly reduced, indicating the effective operation of the active-dummy temperature compensation. Furthermore, the width of these fluctuations decreases as Δf_{rep} is reduced to lower frequencies. A small Δf_{rep} implies that the difference in optical cavity length between the active-sensing OFC and the dummy-sensing OFC is small, indicating that the thermal changes in optical cavity length have a similar impact on both. This is believed to be the origin of this Δf_{rep} dependence. Therefore, a smaller Δf_{rep} is preferred, but there is a limit imposed by the machining precision of the cavity fiber length. For example, the uncertainty of 1 mm in optical cavity length leads to that of 10 kHz in f_{rep1}. The actual machining precision of the fiber cutter is around 1 mm, making it difficult to adjust Δf_{rep} below 1 kHz.

We also investigated the dependence of its frequency instability on Δf_{rep}. Figure 2.6(e) compares the frequency fluctuation among different Δf_{rep} values with respect to gate time. In contrast to Figs. 2.6(a), 2.6(b), 2.6(c), and 2.6(d), no clear Δf_{rep} dependence was observed. This frequency instability reflects short-term rather than long-term behavior, and it was found that Δf_{rep} dependence does not appear on such short time scales. From the viewpoint of RI sensing, the frequency instability in long-term is important.

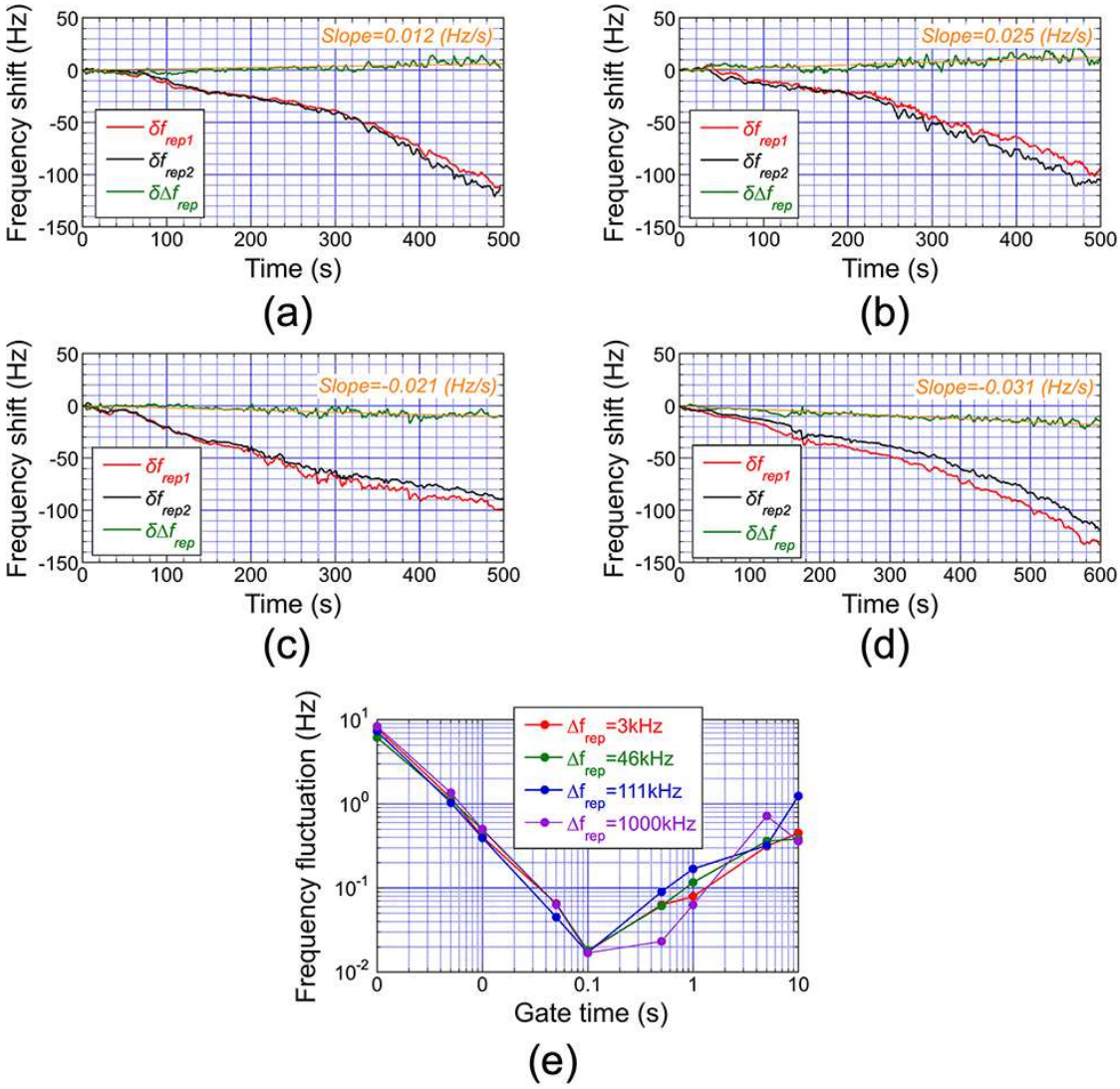

Fig. 2.6. Temporal shifts in f_{rep1}, f_{rep2}, and Δf_{rep} (δf_{rep1}, δf_{rep2}, and $\delta\Delta f_{rep}$) when Δf_{rep} was set to be (a) 3 kHz, (b) 46 kHz, (c) 111 kHz, and (d) 1000 kHz. (e) Comparison of frequency fluctuation among different Δf_{rep} values with respect to gate time.

2.4.3 Dependence of temperature-compensated RI sensing on Δf_{rep}

Finally, we investigated the dependence of active-dummy temperature-compensated RI sensing on Δf_{rep} (= 3 kHz, 40 kHz, 150 kHz, and 1,000 kHz). We used ethanol solutions consisting of water (RI = 1.3180 refractive index unit or RIU at 1550 nm) and ethanol (RI = 1.347 RIU at 1550 nm) at different ratios, corresponding to different RIs, as target samples in the active-sensing OFC. We prepared six samples with different RIs (= 0 EtOH%, 2.5 EtOH%, 5 EtOH%, 7.5 EtOH%, 10 EtOH%, corresponding to 1.3180 RIU, 1.3188 RIU, 1.3196 RIU, 1.3205 RIU, and 1.3213 RIU). Additionally, pure water (a 0 vol% ethanol solution, corresponding to 1.3180 RIU)

was used as a reference material with a constant RI in the dummy-sensing OFC. We repeated the RI sensing of ethanol solutions with different concentrations five times based on the measurement of f_{rep1}. Figure 2.7 shows the average and standard deviation of f_{rep1} measured with different RI samples when Δf_{rep} was set to be (a) 3 kHz, (b) 40 kHz, (c) 150 kHz, and (d) 1000 kHz. While a relatively large standard deviation is observed, the standard deviation varies significantly with Δf_{rep}. The reason for this behavior, which should ideally show similar fluctuations in f_{rep1} regardless of the value of Δf_{rep}, is believed to be due to the behavior of temperature drift, as shown in Fig. 2.5(b). Depending on the timing of the measurement start, f_{rep1} is influenced differently by temperature drift. This results in the difficulty to establish the one-to-one correspondence between f_{rep1} and sample RI.

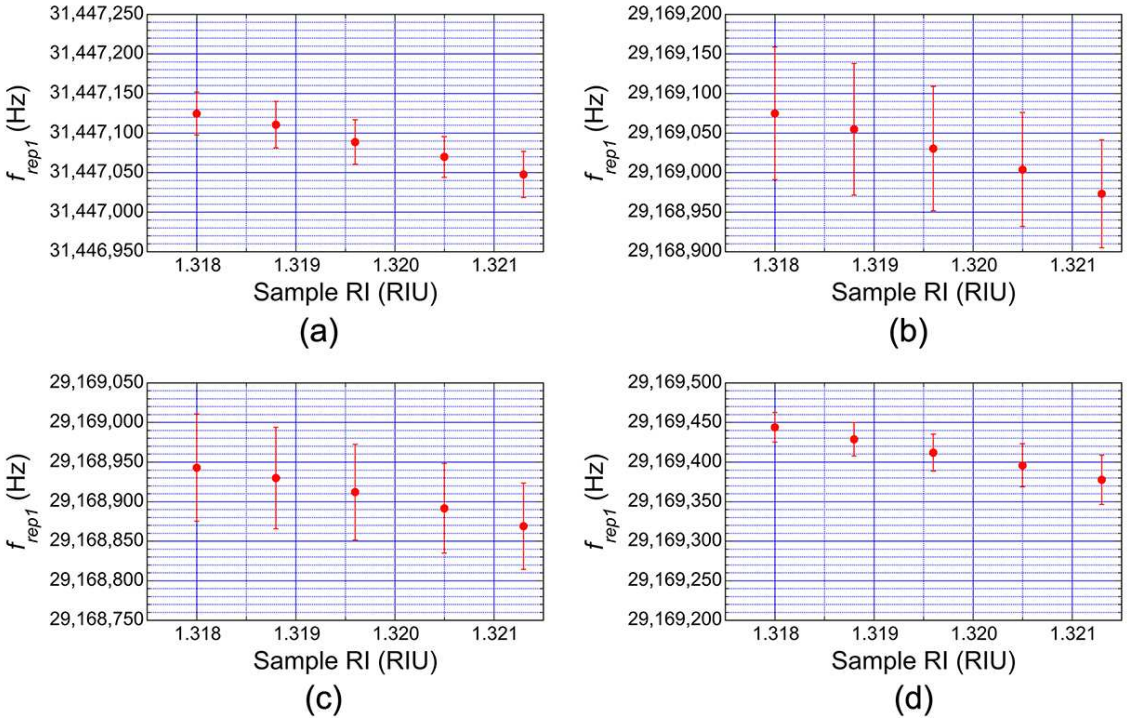

Fig. 2.7. Average and standard deviation of f_{rep1} measured with different RI samples: (a) Δf_{rep} = 3 kHz, (b) Δf_{rep} = 40 kHz, (c) Δf_{rep} = 150 kHz, and (d) Δf_{rep} = 1000 kHz.

We next repeated the RI sensing of ethanol solutions with different concentrations five times based on the measurement of Δf_{rep}. Figure 2.8 shows the average and standard deviation of Δf_{rep} measured with different RI samples when Δf_{rep} was set to be (a) 3 kHz, (b) 40 kHz, (c) 150 kHz, and (d) 1000 kHz. For instance, when Δf_{rep} is 3 kHz, 46 kHz, and 111 kHz, the standard deviation of Δf_{rep} (typically, a few Hz) is significantly smaller than that of f_{rep1} [typically, several tens Hz; see Figs. 2.7(a), 2.7(b), and 2.7(c)]. This indicates that the active-dummy temperature compensation is functioning, and a one-to-one correspondence between Δf_{rep} and sample RI is

established independently of environmental temperature changes. This suggests the potential for RI sensing based on the absolute measurement of Δf_{rep}. However, when Δf_{rep} is 1,000 kHz, the standard deviation of f_{rep1} is equivalent to that of Δf_{rep}. In this case, active-dummy temperature compensation is not functioning. This aligns significantly with the results in Fig. 2.6(d). Thus, we confirmed the dependence of the active-dummy temperature-compensated RI sensing on Δf_{rep}. Since the detailed setting of Δf_{rep} is challenging to achieve below 10 kHz due to the precision of the cavity fiber length machining, it is preferable to choose an optimal value for Δf_{rep} that is 110 kHz or lower, providing some flexibility in the selection process.

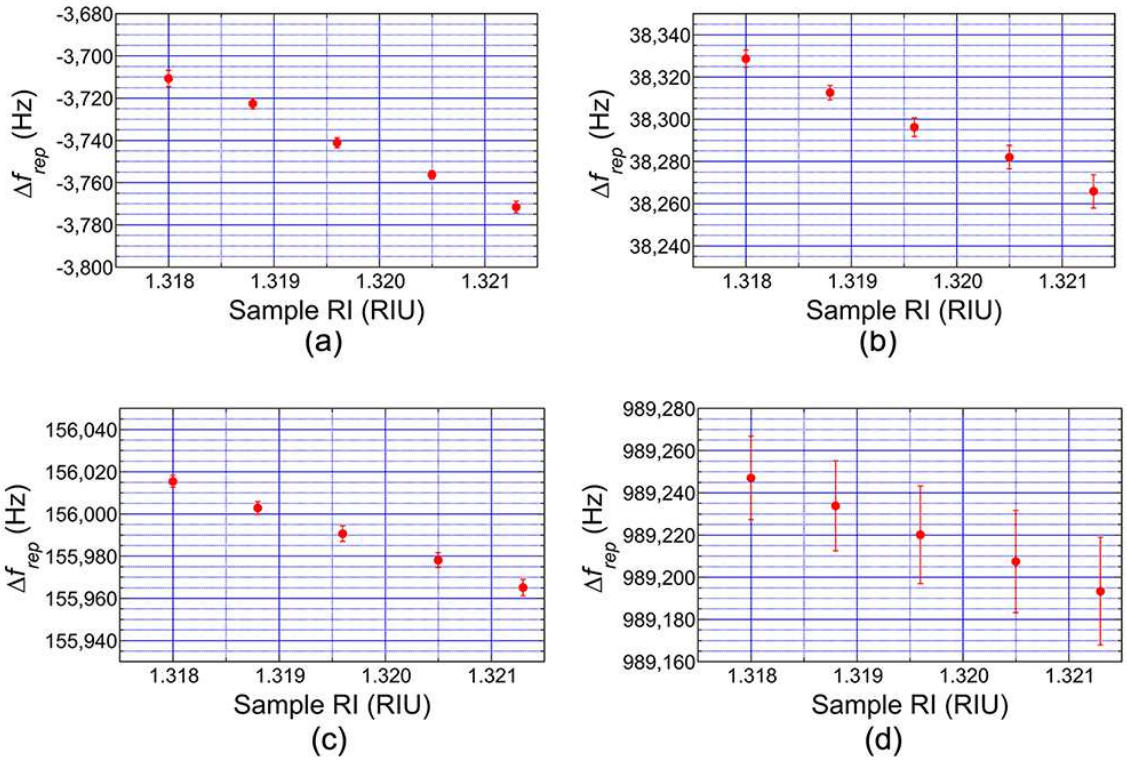

Fig. 2.8. Average and standard deviation of Δf_{rep} measured with different RI samples: (a) Δf_{rep} = 3 kHz, (b) Δf_{rep} = 40 kHz, (c) Δf_{rep} = 150 kHz, and (d) Δf_{rep} = 1000 kHz.

2.5 Discussion

In the active-dummy temperature-compensated RI sensing using a mechanically sharing dual-cavity dual-comb configuration, we have successfully suppressed temperature drift, allowing for absolute RI measurements based on the one-to-one correspondence between Δf_{rep} and sample RI. However, there is still some residual fluctuation in Δf_{rep} that could be further reduced, and here we discuss several challenges for achieving that.

(a) Lower Δf_{rep} values: As shown in Fig. 2.6, reducing Δf_{rep} values improves temperature compensation. However, fine adjustments of Δf_{rep} are limited to a few kHz due to the precision of

cavity fiber length machining. Achieving even lower Δf_{rep} values may be challenging as long as two independent fiber cavities are used. Inserting an optical path length adjustment mechanism using free-space optics into the cavity enables further fine adjustments; however, it may compromise the active-dummy temperature compensation effect.

(b) Spectral overlap of active-sensing and dummy-sensing OFCs: To ensure that the temperature drift of f_{rep1} and f_{rep2} due to thermal changes in the optical cavity length appears similarly in both OFCs, it is essential to have well-overlapped spectra. In the present setup, as shown in Fig. 2.4(a), the spectra of both OFCs did not match closely. This discrepancy could be attributed to slight differences in the characteristics, namely l_{MMI}, of the intracavity MMI fiber sensors, likely due to variations in fiber length machining precision. Achieving further spectral overlap may also be challenging as long as two independent intracavity MMI fiber sensors are used.

(c) Precise alignment of cavity fiber configuration: Another consideration is how accurately the cavity fiber and components can be placed to ensure that both OFCs experience equivalent temperature disturbances. However, there are limits to this alignment, as adjustments need to be made within the confined space of the resonator box.

As such, these three challenges may be challenging with the current experimental setup configuration. To potentially overcome these challenges, one approach could be the use of a single-cavity dual-OFC configuration. Recently, single-cavity dual-comb fiber lasers have gained attention as light sources for dual-comb spectroscopy [33-35]. These fiber lasers achieve dual-comb mode-locked oscillation in a single cavity, resulting in reduced Δf_{rep} fluctuations to below 0.1 Hz without the need for active laser control. This approach has a potential to overcome three challenges above (lower Δf_{rep} values, spectral overlap of active-sensing and dummy-sensing OFCs, and precise alignment of fiber configuration). Although integrating an MMI fiber sensor into such lasers is technically demanding, this combination could significantly enhance the performance of dual-comb RI-sensing while simplifying the experimental setup. Please note that further exploration and experimentation may be required to determine the feasibility and effectiveness of these approaches.

3. Rapid, high-sensitivity detection of biomolecules using dual-comb biosensing

3.1 Introduction

Biosensors are biomolecular sensors that utilize or imitate the skillful molecular identification function of living organisms; they are applied to a wide range of fields such as medical care, food industry, and environmental monitoring. Yet, further enhancement of biosensing performance is still required in the field of infectious pathogens as well as biomarkers, pollutant, bacteria, and environmental hormones. For example, one timely and urgent application that benefits from improved performance is still testing of coronavirus disease 2019 (COVID-19) because COVID-19, caused by severe acute respiratory syndrome coronavirus 2 (SARS-CoV-2), has rapidly spread and is still occurring all over the world. While reverse-transcription polymerase chain reaction (RT-PCR) [36-38] has been widely used as a current standard for COVID-19 testing in clinical practice, research has also been conducted on biosensors of SARS-CoV-2, vigorously. The potential methods that may improve the biosensing performance is the use of optical biosensors [39,40] due to both rapidity and high sensitivity. For example, optical biosensors based on surface plasmon resonance (SPR) [41,42] have been widely used for analyzing biomolecules and viruses; in this technique, the spectral shift of the SPR trough in the wavelength or angular spectrum is measured because the spectral shift depends on a sample concentration due to a combined effect of SPR and molecular identification function on the sensor surface. SPR analysis enables the real-time, label-free analysis of intermolecular interaction or combination by measuring a sample-concentration-dependent optical spectral shift; thus, this technique has been widely applied for the detection of various infectious pathogens as well as various biomarkers [43-55]. The limit of detection (LOD) for SARS-CoV-2 nucleocapsid protein (N protein) antigen has reached 85 fM or 4 pg/ml [49]; however, in order to measure clinical samples (for example, human nasopharyngeal aspirates), further improvement in LOD (to the fM level or sub-fM level) is necessary. A reason for the limited sensitivity in SPR is an optical instrumentation resolution as well as a relatively broad spectrum of SPR trough compared to its slight spectrum shift. Optical biosensing techniques, such as fluorescence [56,57] and surface-enhanced Raman scattering (SERS) [58,59], could be another potential candidate for the biosensing of SARS-CoV-2. For instance, a combination of SERS with antibody pair, SERS-active hollow Au nanoparticles, and magnetic beads achieved LOD of 2.56 fg/mL for the SARS-CoV-2 antigen, facilitating the identification of SARS-CoV-2 in human nasopharyngeal aspirates within 30 min. While the discrimination of infection has been achieved, the Raman signals of samples diagnosed as negative still show variations among samples, which may lead to potential misdiagnosis between false positive and true negative during the early stages of infection.

Regarding the limitation of optical instrumentation resolution in SPR, if this sample-concentration-dependent optical spectral shift is transformed into a photonic radio-frequency (RF) signal, then such photonic RF biosensing would benefit from the high precision and real-time nature provided by well-established electric frequency measurements with RF frequency standards and measurement apparatuses. Recently, optical frequency combs (OFCs) [12-14,80] have attracted attention for use as photonic RF sensors based on a frequency conversion function between the optical and RF regions [22,23]. OFC is composed of a series of optical frequency modes (freq. = n_m) with a constant mode spacing of f_{rep} in the RF band. A relation between n_m and f_{rep} is given by

$$\nu_m = f_{ceo} + mf_{rep,} \tag{1}$$

where f_{ceo} is a carrier-envelope-offset frequency and m is mode number. Since f_{rep} is a RF signal, OFC acts as an accurate frequency converter between optical and electrical regions. For example, a refractive-index-dependent (RI-dependent) optical spectrum shift was converted into a change in f_{rep} of around several tens of MHz by placing a multimode-interference (MMI) fiber sensor [27,81] inside a fiber OFC cavity. Then, the f_{rep} signal with the spectral linewidth below 1 Hz [28] was rapidly and precisely measured by a RF frequency counter. Furthermore, the intracavity fiber sensor enables multiple interactions between the sample and the light, enhancing the sensitivity. Due to the precise electric-measurement of the narrow-linewidth, sensitivity-enhanced f_{rep} signal, this RI-sensing OFC enables precise measurement of the sample RI with a resolution of 4.88×10^{-6} refractive index units (RIU), which is two orders of magnitude better than that of the previous study of RI sensing with MMI fiber sensor [27]. Such high-sensitivity RI-sensing OFCs would have the potential to be further extended to optical biosensing, namely, to biosensing OFCs, through surface modification of the MMI fiber sensor with the molecular identification layer in terms of biomolecule interactions, similar to the surface modification employed in SPR. However, there are no attempts to apply this RI-sensing OFC for optical biosensing because the residual temperature drift of the f_{rep} signal (typically, a few hundreds Hz/hour) is still larger than the sample-concentration-dependent f_{rep} shift in biosensing (typically, a few to a few tens Hz), reducing the precision and hindering its extension to the biosensing OFC. It is essential to largely reduce the temperature drift of f_{rep} in order to open the door for the biosensing OFC.

Thus, in this chapter, we first developed a dual-comb configuration with an active sensing OFC and a dummy sensing OFC to suppress the temperature drift of the f_{rep} signal, namely, dual-comb biosensing; this function is similar to the active-dummy temperature compensation of strain sensors. Then, for preliminarily test of dual-comb biosensing, we applied the active-dummy dual sensing OFCs to RI sensing of a glycerol solution, which is a stable standard substance without

volatilization. Finally, for proof of concept using biomolecules, we demonstrate rapid detection of the SARS-CoV-2 N protein antigen by combining the active-dummy dual sensing OFCs and surface modification of a SARS-CoV-2 N protein antibody. Prior to using real samples of SARS-CoV-2, to assess the net performance of dual-comb biosensing alone without the help of specific enhancing techniques regarding antigen-antibody interactions and/or surface modifications, commercially available, purified SARS-CoV-2 N protein antigen diluted in phosphate-buffered saline (PBS) was detected by a help of a commercially available SARS-CoV-2 N protein antibody. Since the dual-comb biosensing can be implemented with a wide variety of surface modifications for other viruses/pathogens and biological molecules, it greatly enhances the applicability of optical biosensors for virus, bacteria, protein, biomarker, environmental hormone, and so on.

3.2 Results

3.2.1 General principle of operation

In this study, we sought to design a biosensor that combines photonic-to-RF conversion and antigen-antibody interaction in an OFC. The biosensing OFC operates through three steps: Step (1) antigen-antibody interactions on the antibody-modified sensor surface, Step (2) RI-dependent optical spectrum shift of OFC provided by the intracavity MMI fiber sensor, and Step (3) photonic-to-RF conversion by the wavelength dispersion of the fiber cavity, as depicted in Fig. 3.1(a). In Step (1), the selective combination of a target antigen with the corresponding antibody changes the effective RI near the sensor surface depending on the antigen concentration. In Step (2), since the intracavity MMI fiber sensor transmits only certain wavelength (λ_{MMI}) light based on its RI due to MMI and the Goos-Hänchen shift, the OFC shows an RI-dependent and hence an antigen-concentration-dependent shift in the optical spectrum. Simultaneously, the intracavity MMI fiber sensor enhances the sensing sensitivity by multiple interactions between light and sample inside the OFC cavity. The functions of Steps (1) and (2) are implemented by an intracavity MMI fiber sensor with antibody surface modification, as shown in Fig. 3.1(b). In Step (3), the antigen-concentration-dependent shift in the optical spectrum is converted to a shift in the optical cavity length nL, where n and L are the RI and the physical length of the OFC cavity fiber, via the wavelength dispersion of RI in the cavity fiber. Finally, the change in the antigen concentration can be read out as the f_{rep} shift via $f_{rep} = c/nL$, where c is the velocity of light in a vacuum. Importantly, the f_{rep} linewidth achieves down to below 1 Hz, which is smaller than f_{rep} shift expected due to the antigen concentration change.

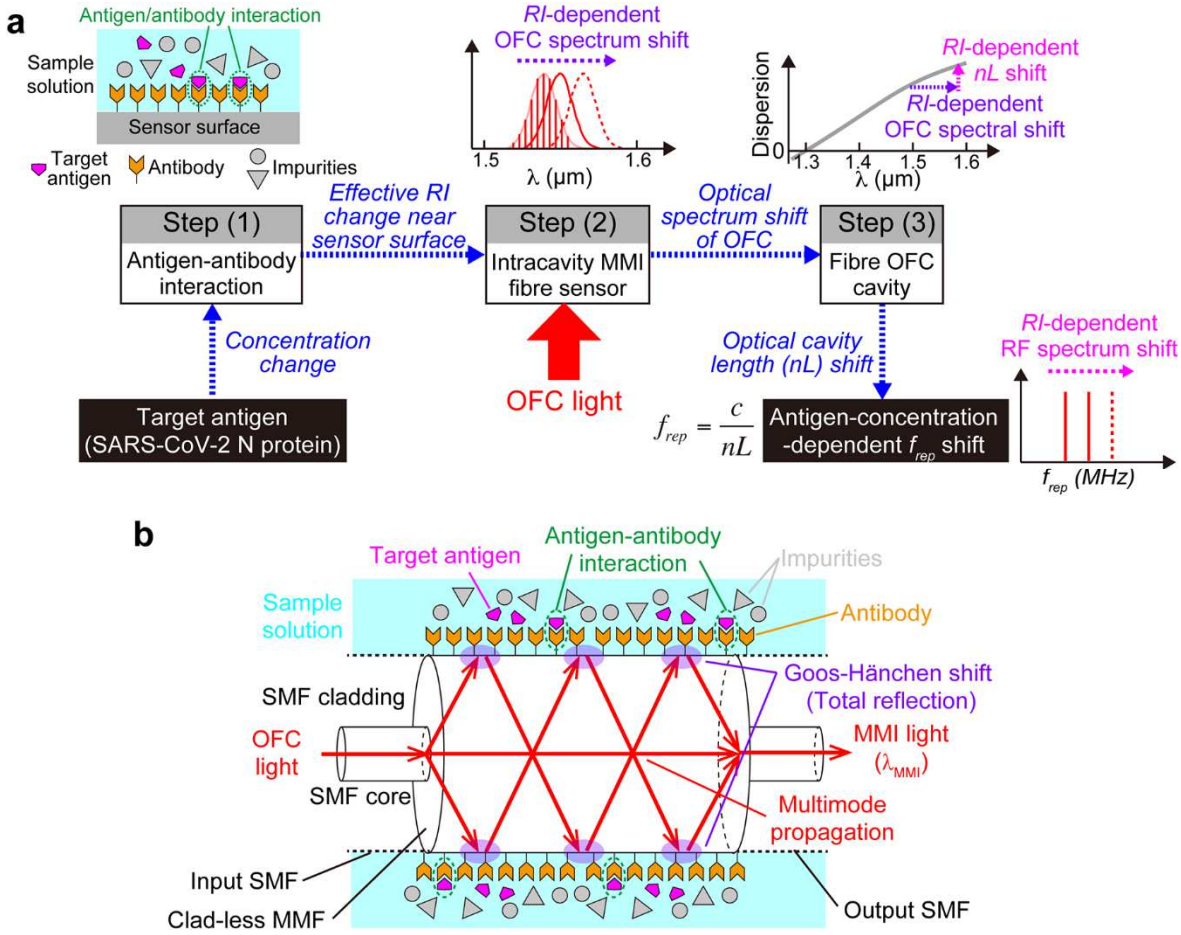

Fig. 3.1. Principle of operation for the biosensing OFC. (a) Block diagram of the signal flow. The concentration of the target antigen is obtained according to the mode spacing f_{rep} of the OFC through three steps: Step (1) antigen-antibody interactions on the antibody-modified sensor surface, Step (2) RI-dependent optical spectrum shift of OFC provided by the intracavity MMI fiber sensor, and Step (3) photonic-to-RF conversion by the wavelength dispersion of the fiber cavity. (b) Schematic diagram of the intracavity MMI fiber sensor with antibody surface modification. The antigen-antibody interaction on the surface of the intracavity MMI fiber sensor is reflected by an effective RI change near the sensor surface, while the intracavity MMI fiber sensor functions as an RI-dependent variable-optical-bandpass filter via the MMI process. The combination of the antigen-antibody interaction with the MMI fiber sensor causes an antigen-concentration-dependent optical spectrum shift of OFC.

3.2.2 Temperature drift in the single-comb configuration

We first evaluated the dependence of f_{rep} in a single sensing OFC on cavity temperature because the temperature disturbance to the fiber OFC cavity fluctuates f_{rep} via thermal expansion

or shrinkage of *nL*. To this end, we measured the temporal drift in the f_{rep} of the single-comb configuration of sensing OFC under an uncontrolled cavity temperature, as shown in Fig. 3.2(a), whose details are given in the Materials and Methods section. We set the center optical wavelength λ_{MMI} of 1556.6 nm and the frequency spacing f_{rep} of 31.7 MHz for stable mode-locked oscillation with the intracavity MMI fiber sensor. Pure water was used for a standard sample with a stable RI, and placed in a glass sample cell together with the MMI fiber sensor without the surface modification for RI sensing. The output light from the OFC was detected by a photodetector (PD), and f_{rep} was measured by an RF frequency counter synchronized to a rubidium frequency standard working in the RF band. Figure 3.2(b) shows the f_{rep} shift (δf_{rep}, blue line) when the cavity temperature (orange line) changed over a range of 1 °C. δf_{rep} represents the frequency deviation from the initial measurement value. The temporal behavior of δf_{rep} in synchronization with the cavity temperature indicated a temperature sensitivity of approximately -400 Hz/°C. Thus, the cavity-temperature-dependent f_{rep} drift is considerably larger than the sample-concentration-dependent f_{rep} shift in biosensing (typically, a few to a few tens Hz). Although the cavity temperature could be actively controlled within a range of 0.1 °C, it is still insufficient to suppress the cavity-temperature-dependent f_{rep} drift (= 400 Hz/°C × 0.1 °C = 40 Hz) below the sample-concentration-dependent f_{rep} shift. Thus, to further reduce the temperature drift, we applied a dual-comb configuration for active-dummy compensation of the temperature drift as described in the following subsection.

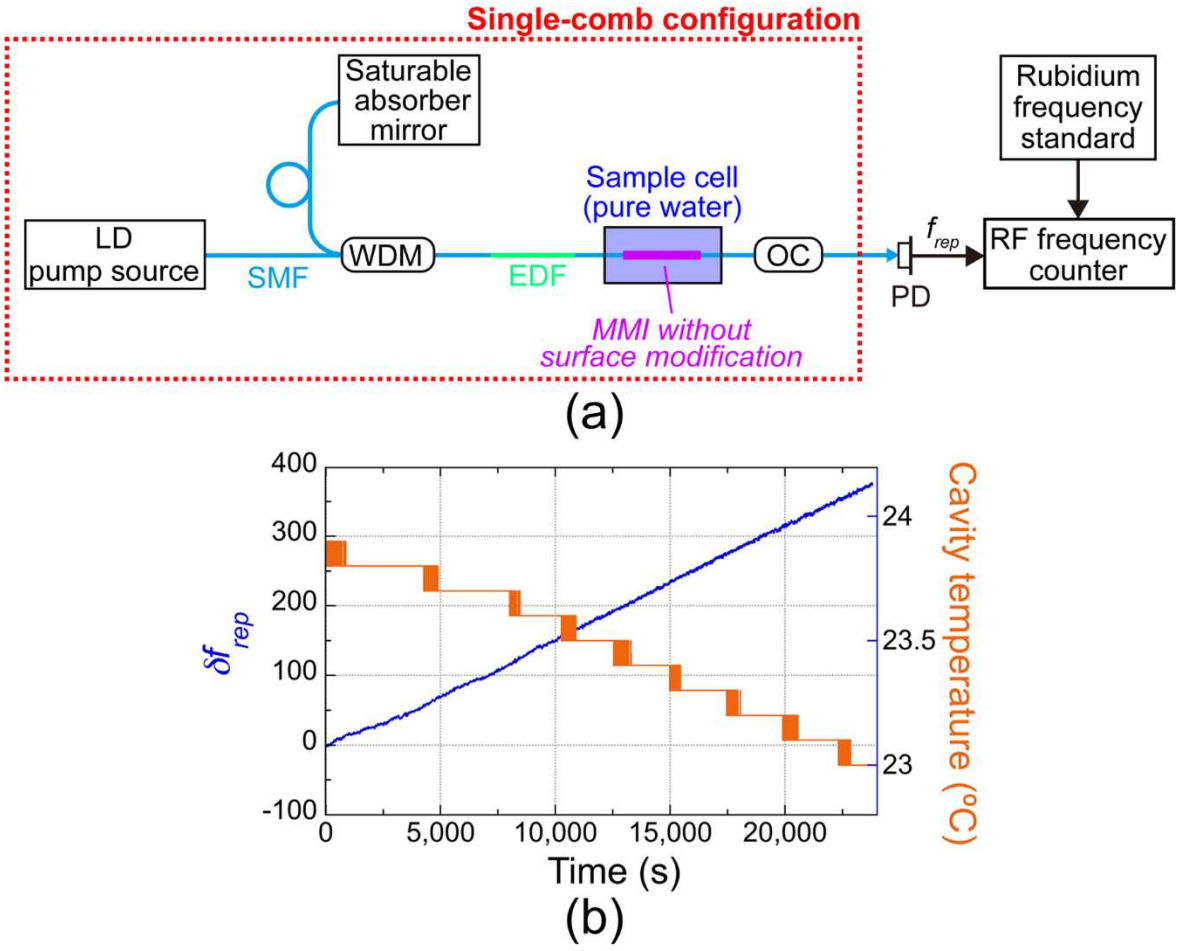

Fig. 3.2. Basic performance of single-comb RI sensing of pure water with temperature drift. (a) Schematic drawing of the experimental setup. LD, laser diode; SMF, single-mode fiber; WDM, wavelength-division-multiplexing coupler; EDF, erbium-doped fiber; MMI, multimode-interference fiber sensor; OC, fiber output coupler; PD, photodiode. Details of the single sensing OFC are given in the Materials and Methods section. (b) Temporal drift of the cavity temperature (orange line) and the corresponding f_{rep} shift (δf_{rep}, blue line). Pure water was used as the sample of RI sensing. δf_{rep} was calculated as the frequency deviation from the initial value of f_{rep}. The stepped-down behavior of the cavity temperature is due to the temperature resolution of the thermistor (= 0.1 °C) used for monitoring the cavity temperature. The cavity temperature sensitivity of the single sensing OFC was approximately -400 Hz/°C.

3.2.3 Active-dummy compensation of the temperature drift with the dual-comb configuration

A dual-comb configuration with an active sensing OFC with a frequency spacing of f_{rep1} and a dummy sensing OFC with a frequency spacing of f_{rep2} was adopted to compensate for the temperature drift. Figure 3.3(a) shows a schematic drawing of the dual-comb configuration, in

which a pair of fiber OFC cavities were arranged in an aluminum box covered by insulated materials so that they were affected by similar temperature drifts. In this configuration, although f_{rep1} and f_{rep2} fluctuate depending on the residual drift of cavity temperature via thermal expansion or shrinkage of nL, their drifts are similar because they experience the same thermal disturbances. Therefore, the frequency difference Δf_{rep} between f_{rep1} and f_{rep2} remains constant regardless of the temperature drift of f_{rep1} and f_{rep2}. Thus, when the active sensing OFC evaluates a sample solution in a certain temperature environment and the dummy sensing OFC evaluates a reference material in the same temperature environment, Δf_{rep} reflects the sample concentration without influence from temperature drift. In other words, a one-to-one correspondence between Δf_{rep} and the sample concentration is established independent of temperature drift. Figures 3.3(b), 3.3(c), and 3.3(d) show the MMI and sample cell for dual-comb RI sensing of pure water, dual-comb RI sensing of glycerol solution, and dual-comb biosensing of the SARS-CoV-2 N protein antigen, respectively. Table 3.1 summarizes λ_{MMI}, f_{rep1}, f_{rep2}, Δf_{rep}, the MMI, and the sample cell used in the following three dual-comb sensing experiments; these values were selected for stable operation and better temperature compensation. A pair of output lights from the active and the dummy sensing OFCs is detected by a pair of photodetectors (PDs). Their frequency signals (= f_{rep1} and f_{rep2}) and a frequency difference between them (= $\Delta f_{rep} = f_{rep1} - f_{rep2}$) are measured by the RF frequency counter. Details of the dual-comb biosensing technique are given in the Materials and Methods section, together with details on the experimental and analytical methodology employed for all measurements.

Table 3.1. Experimental settings of dual-comb RI sensing and biosensing.

Experiments	λ_{MMI} (nm)	f_{rep1} (MHz)	f_{rep2} (MHz)	Δf_{rep} (kHz)	Active MMI	Dummy MMI	Sample cell
Dual-comb RI sensing of pure water	1556.6	31.7	32.5	-851.9	No surface modification		Single [Fig. 3.3(b)]
Dual-comb RI sensing of glycerol solution	1556.6	31.7	32.5	-851.9	No surface modification		Dual [Fig. 3.3(c)]
Dual-comb biosensing of SARS-CoV-2 N protein antigen	1556.6	29.6	29.7	-88.6	Surface modification of antibody	No surface modification of antibody	Single [Fig. 3.3(d)]

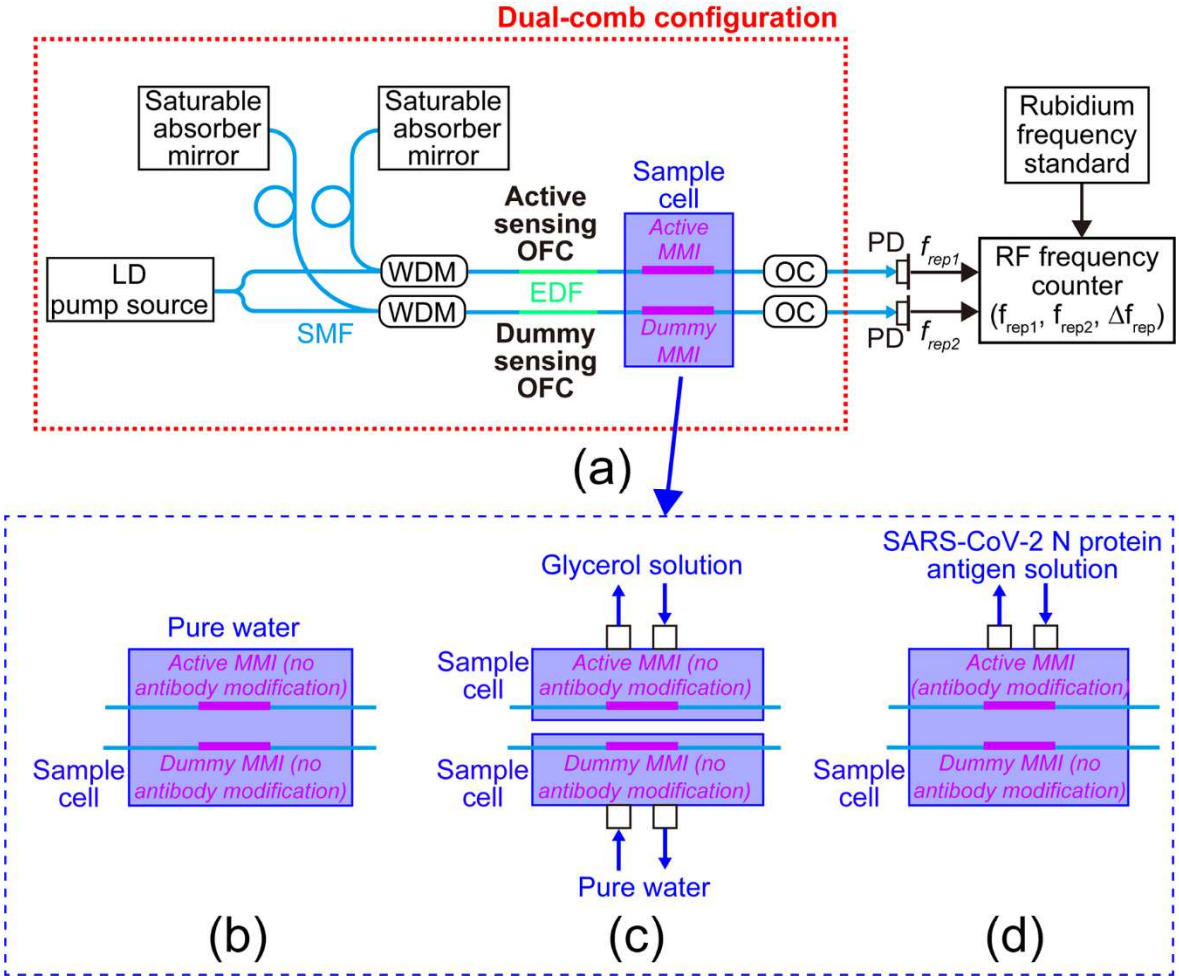

Fig. 3.3. Experimental setup of dual-comb RI sensing and biosensing. (a) Schematic drawing of the whole experimental setup. LD, laser diode; SMFs, single-mode fibers; OFCs, optical frequency combs; WDMs, wavelength-division-multiplexing couplers; EDF, erbium-doped fiber; active MMI, intracavity multimode-interference fiber sensor for a target sample; dummy MMI, intracavity multimode-interference fiber sensor for a reference sample; OCs, fiber output couplers; PDs, photodiodes. The active sensing OFC and dummy OFC operate at a center optical wavelength (λ_{MMI}) of 1556.6 nm. (b) Schematic drawing of the MMI sensor and sample cell for dual-comb RI sensing of pure water. (c) Schematic drawing of the MMI sensor and sample cell for dual-comb RI sensing of glycerol solution. (d) Schematic drawing of the MMI sensor and sample cell for dual-comb biosensing of the SARS-CoV-2 N protein antigen solution. Peristaltic pumps were used for sample exchange in the dual-comb RI sensing of glycerol solution and the dual-comb biosensing of the SARS-CoV-2 N protein antigen.

The blue and green lines in Fig. 3.4 show the temporal shifts in f_{rep1} and f_{rep2}, namely, δf_{rep1} and δf_{rep2}, respectively, when pure water was used as a sample for both the active and dummy sensing OFCs without surface modification [see the second row in Table 3.1 and Fig. 3.3(b)]. δf_{rep1} and δf_{rep2} suffered from a frequency drift of over -38 Hz, implying a temperature drift of 0.1 °C during the data acquisition from a temperature sensitivity of -400 Hz/°C in Fig. 3.2(b). However, importantly, δf_{rep1} and δf_{rep2} behaved almost the same in terms of drift. The resulting Δf_{rep} shift ($\delta\Delta f_{rep}$) was stable as shown by the red line in Fig. 3.4, in which the standard deviation of $\delta\Delta f_{rep}$ was 0.066 Hz at 10 s, 0.209 Hz at 100 s, and 0.177 Hz at 1000 s, respectively. These variations are equivalent to a temperature stability of 1.64×10^{-4} °C at 10 s, 5.23×10^{-4} °C at 100 s, and 4.42×10^{-4} °C at 1000 s, much better than that by the temperature controller of fiber OFC cavity.

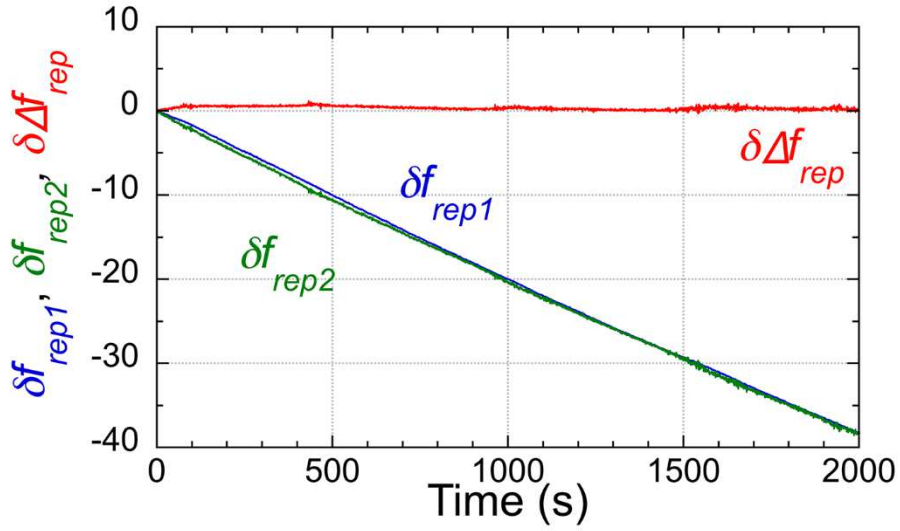

Fig. 3.4. Basic performance of dual-comb RI sensing of pure water with temperature drift. Temporal drifts in δf_{rep1}, δf_{rep2}, and $\delta\Delta f_{rep}$ when pure water was used as a sample for the active and dummy RI-sensing OFCs [see Table 3.1 and Fig. 3(b)]. δf_{rep1}, δf_{rep2}, and $\delta\Delta f_{rep}$ were calculated as the frequency deviations from the initial values of f_{rep1}, f_{rep2}, and Δf_{rep}, respectively.

We next tested active-dummy temperature compensation for RI sensing of a liquid sample different from the reference sample. For RI sensing, the active and dummy sensing OFCs have no surface modification in MMI [see the third row in Table 3.1 and Fig. 3.3(c)]. We used glycerol solutions consisting of glycerin and pure water at different ratios, corresponding to different RIs, as target samples in the active sensing OFC. This sample is easy to prepare and stable as it does not volatilize. We prepared six samples with different RIs [= 0 vol%, 1 vol%, 2 vol%, 3 vol%, 4 vol%, and 5 vol%, corresponding to 1.3165 RIU, 1.3179 RIU, 1.3193 RIU, 1.3207 RIU, 1.3222

RIU, and 1.3236 RIU; see color-highlighted zones in Figs. 3.5(a) and 3.5(b)] because their expected f_{rep} shift is comparable to the concentration-dependent f_{rep} shift caused by the SARS-CoV-2 N protein antigen. The RI of the sample was calculated from the volume ratio of water (RI = 1.3165 RIU at 1550 nm) and glycerin (RI = 1.4571 RIU at 1550 nm). While our experiments were conducted in volume ratio (vol%) of glycerin-water solutions, the correlation in the literature were provided in terms of weight ratio (wt%). To address this discrepancy, we performed a conversion between vol% and wt% by using the volume and density (=1.26) of 100% glycerin to calculate the corresponding weight, and then dividing it by the weight of water. This process yielded the weight ratio. Subsequently, we employed this weight ratio to calculate the RI value of each sample based on the RI values from the literature. We exchanged the sample by using a peristaltic pump [see grey zones in Figs. 3.5(a) and 3.5(b)]. Additionally, pure water (a 0 vol% glycerol solution, corresponding to 1.3165 RIU) was used as a reference sample in the dummy sensing OFC. To prevent the temperature of the pure water in the dummy sample cell from increasing during repeated measurements, the pure water sample was exchanged with a new pure water sample with another peristaltic pump when the target sample was exchanged with a new RI glycerol sample. The blue and green lines in Fig. 3.5(a) represent δf_{rep1} and δf_{rep2} as the concentration of the glycerol solution increased from 0 vol% to 5 vol%. δf_{rep2}, in the dummy sensing OFC, exhibited a slow drift with some rapid changes even though the RI of the pure water was constant. This slow drift is due to the temperature drift, too. Since rapid changes in δf_{rep2} were synchronized with the operation of the peristaltic pump, they are caused by disturbance from the water flow when the samples were exchanged. In contrast, δf_{rep1}, in the active sensing OFC, exhibited a combination of a step-like change with the sample RI and the slow drift shown by δf_{rep2} together with rapid changes. This combination of behavior in δf_{rep1} is detrimental to the RI sensing performance in the single sensing OFC configuration. The behavior of rapid changes caused by the peristaltic pump is different between δf_{rep1} and δf_{rep2} because the shape of the two separate sample cells is not identical, and the position of the MMI fiber sensors in those cells is not completely the same.

Figure 3.5 (b) shows a sensorgram of $\delta\Delta f_{rep}$ calculated by subtracting the green line (δf_{rep2}) from the blue line (δf_{rep1}) in Fig. 3.5 (a). The temperature drift almost disappeared, and only the step-like change with the sample RI was present in $\delta\Delta f_{rep}$. The mean and the standard deviation of $\delta\Delta f_{rep}$ were 0.76±0.19 Hz at 0 vol% or 1.3165 RIU, -7.58±0.24 Hz at 1 vol% or 1.3179 RIU, -16.48±0.52 Hz at 2 vol% or 1.3193 RIU, -25.64±0.53 Hz at 3 vol% or 1.3207 RIU, -34.59±0.31 Hz at 4 vol% or 1.3222 RIU, and -43.12±0.34 Hz at 5 vol% or 1.3236 RIU, as shown by red plots in Fig. 3.5(c). From these values, we calculated a relation between the sample RI and $\delta\Delta f_{rep}$. The linear relation between the sample RI and $\delta\Delta f_{rep}$ was obtained with a correlation coefficient (R)

of 0.9999. The good fitting result indicated that the dual-comb effect minimizes the effect of temperature drift. From the slope coefficient of the linear fitting (= -6216 Hz/RIU) and the stability of $\delta\Delta f_{rep}$ (= 0.198 Hz at 10 s, 0.627 Hz at 100 s, and 0.531 Hz at 1000 s based on three times the standard deviation), the RI resolution was determined to be 3.19×10^{-5} RIU at 10 s, 1.01×10^{-4} RIU at 100 s, and 8.54×10^{-5} RIU at 1000 s. In RI sensing of a liquid sample (glycerol solutions) different from another liquid reference (pure water), difference of thermo-optic effect between them may influence the effective RI and the temperature sensitivity because they have inherent thermo-optic coefficients (typically, 10^{-4} RIU/°C at 1550 nm) [82,83]. When their temperature is stable within a range of 0.1 °C, the drift of RI in the sample and the reference is estimated to be the order of 10^{-5} RIU. However, the temporal drift of thermo-optic coefficients will be common to each other if similar water solutions refer to the solutions used in the following measurements, and the active-dummy temperature compensation can work well. Therefore, the effect of different thermo-optic effects is negligible.

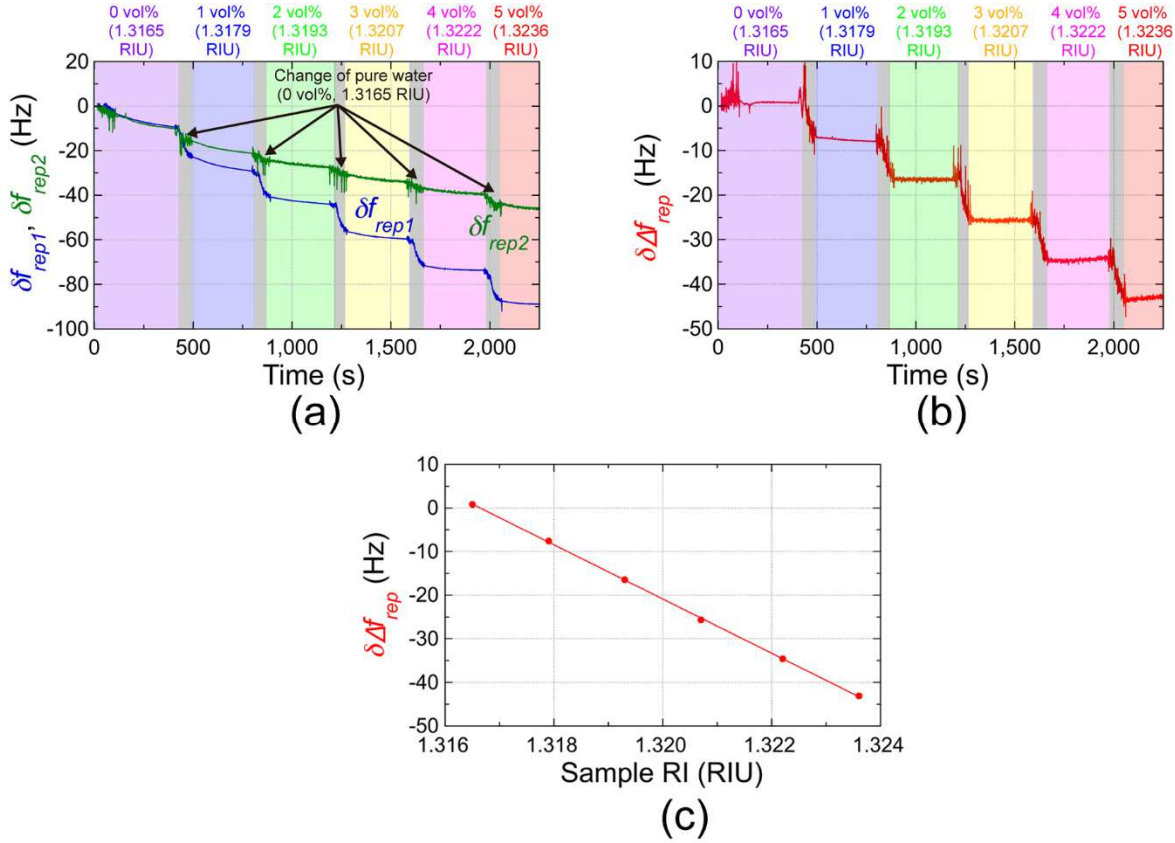

Fig. 3.5. Temperature-drift-free dual-comb RI sensing of glycerol solution. (a) Sensorgrams of δf_{rep1} in the active sensing OFC and δf_{rep2} in the dummy sensing OFC. Glycerol solutions consisting of glycerin and pure water at different ratios were used as the target samples in the active sensing OFC; pure water was used as the reference sample in the dummy sensing OFC [see

Table 3.1 and Fig. 3.3(c)]. Grey zones indicate the time period for sample exchange by peristaltic pumps. δf_{rep1} and δf_{rep2} were calculated as the frequency deviations from the initial values of f_{rep1} and f_{rep2}, respectively. (b) Sensorgram of $\delta \Delta f_{rep}$ with mixtures of glycerin and pure water at different ratios. $\delta \Delta f_{rep}$ was calculated as the frequency deviation from the initial value of Δf_{rep}. (c) Relationship between the sample RI and $\delta \Delta f_{rep}$.

3.2.4 Rapid detection of SARS-CoV-2 N protein antigen

Antibody modification of the intracavity MMI fiber sensor creates a photonic RF biosensor for the detection of target antigens through antibody-antigen reactions because the RI-dependent f_{rep} shift is converted into an antigen-concentration-dependent f_{rep} shift [see Fig. 1(a)]. We confirmed the effectiveness of the active-dummy compensation with the dual-comb configuration in high-precision RI sensing demonstrated above. The resulting enhanced RI precision covers the effective RI change expected by the antigen-antibody interaction on the sensor surface, enabling us to apply these dual sensing OFCs for rapid, high-sensitive detection of viruses/pathogens and biological molecules.

The concept of the antigen-antibody interaction (in this case, a viral protein) was applied for the detection of SARS-CoV-2 protein with dual-comb biosensing. Among several proteins in SARS-CoV-2, we selected the N protein instead of the well-known and peculiar spike protein for antigen-antibody interactions. This is because the N protein functions to package the viral RNA genome within the viral envelope into a ribonucleoprotein complex and has benefits such as abundance, low probability of mutation, and relatively low molecular weight. We used a pair of a commercialized N protein antibody (Fapon Biotech Inc., Dongguan, Guangdong, China, FPZ0553) and a commercialized recombinant N protein antigen (Fapon Biotech Inc., Dongguan, Guangdong, China, FPZ0513) for antigen-antibody interactions in the intracavity MMI biosensor [see Fig. 3.1(b)]. Before performing the dual-comb biosensing, we evaluate the affinity of this pair by enzyme-linked immunosorbent assay (ELISA). Figure 3.6 shows a relation between antigen concentration and optical density at 450 nm, indicating a sensitivity within a range of 10 pM to 10 nM in ELISA. We made a surface modification of the MMI fiber sensor (material = SiO_2) with amino-terminated groups through a silane coupling reaction for a self-assembled monolayer (SAM) after surface cleaning and modifying by UV ozone. Then, the N protein antigen was immobilized on the amino-group-coated MMF fiber sensor surface to realize an active sensing OFC. Additionally, the SAM without immobilized antibody was applied to the surface of the MMI fiber sensor for the dummy sensing OFC. The MMI fiber sensors with and without surface modification by the immobilized antibody were placed together in the same sample cell for the active and dummy sensing OFCs, respectively [see the last row in Table 3.1 and Fig.

3.3(d)]. Solution samples of the N protein antigen in phosphate-buffered saline (PBS) at different molar concentrations were consecutively introduced into the sample cell with a peristaltic pump. The N protein antigen-antibody interaction could only occur on the sensor surface of the active sensing OFC because that of the dummy sensing OFC did not include immobilized antibodies. Thus, the dummy sensing OFC was used for the compensation of temperature drift assuming that non-specific adsorption did not occur on the sensor surface of the dummy sensing OFC.

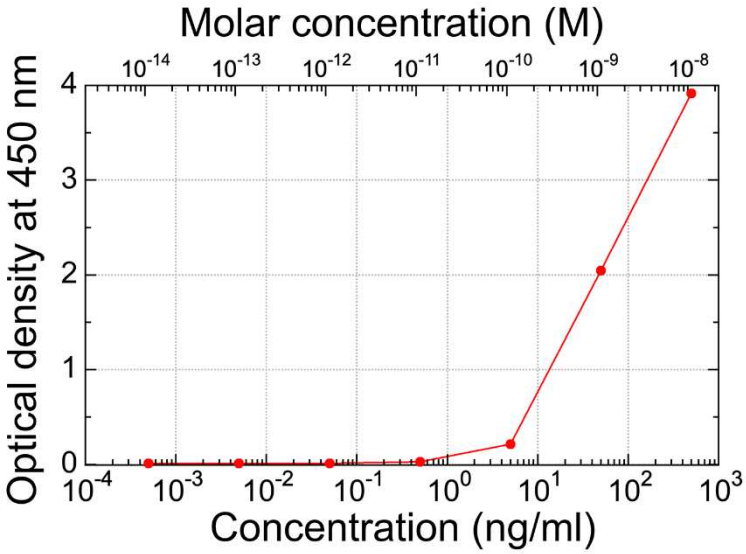

Fig. 3.6. Affinity test between a commercialized antibody (FPZ0553, Fapon Biotech Inc.) and a commercialized antigen (FPZ0513, Fapon Biotech Inc.) for SARS-CoV-2 N protein by ELISA.

Figure 3.7(a) shows the sensorgram of δf_{rep1} and δf_{rep2} as the molar concentration of the antigen/PBS solution increased from 1 aM (blue zone), 1 fM (green zone), 1 pM (yellow zone), and 1 nM (red zone) after starting with pure PBS (purple zone). We here selected the considerably wide range of molar concentrations for the initial evaluation of basic performance in dual-comb biosensing of SARS-CoV-2 N protein antigen. The precise evaluation focused within the clinically-relevant range of SARS-CoV-2 N protein antigen will be the future work. The time period for data acquisition [see color-highlighted zones in Fig. 3.7(a)] was set to 10 min. In the grey zones (time period = 8 min), we performed the following three steps: (1) we introduced the antigen/PBS solution into the sample cell with the peristaltic pump (1.5 min), (2) we waited for the antigen-antibody interaction to be completed (5 min), and (3) we rinsed the sensor surface with PBS to flush the accumulated N protein antigen that did not interact with the antibodies away (1.5 min). When the antigen was washed with the PBS buffer after being added and waited, the sensor signal reflects the amount of the antigen adsorbed on the sensor surface after desorption. However, the step-like change in δf_{rep1} with the antigen concentration was completely

overshadowed by the background temperature drift. So, we next calculated the frequency difference ($\delta\Delta f_{rep}$) between δf_{rep1} and δf_{rep2} to eliminate the influence of temperature drift as described in the previous subsection. Figure 3.7(b) shows the sensorgram of $\delta\Delta f_{rep}$. Focusing on the zones highlighted in colors other than grey, a slightly dull stepped change in $\delta\Delta f_{rep}$ dependent on the molar concentration was observed, although a small drift in $\delta\Delta f_{rep}$ within the range of a few Hz remained at each molar concentration. To evaluate the validity of this behavior in the sensorgram, we calculated the mean and the standard deviation of $\delta\Delta f_{rep}$ at each molar concentration (each color zone other than grey zones): -1.42±1.00 Hz at 1 aM, -8.82±0.57 Hz at 1 fM, -24.29±0.36 Hz at 1 pM, and -27.52±1.08 Hz at 1 nM, respectively. They are indicated as red circles and corresponding error bars in Fig. 3.7(c). The negative slope was consistent with the RI dependence of $\delta\Delta f_{rep}$ [see the red line plotted in Fig. 3.5(c)] because the progression of the antigen-antibody reaction increases the effective RI near the MMI fiber sensor and hence decreases f_{rep} [66]. In this way, we demonstrated the potential for rapid detection of the SARS-CoV-2 N protein antigen within this range of molar concentrations.

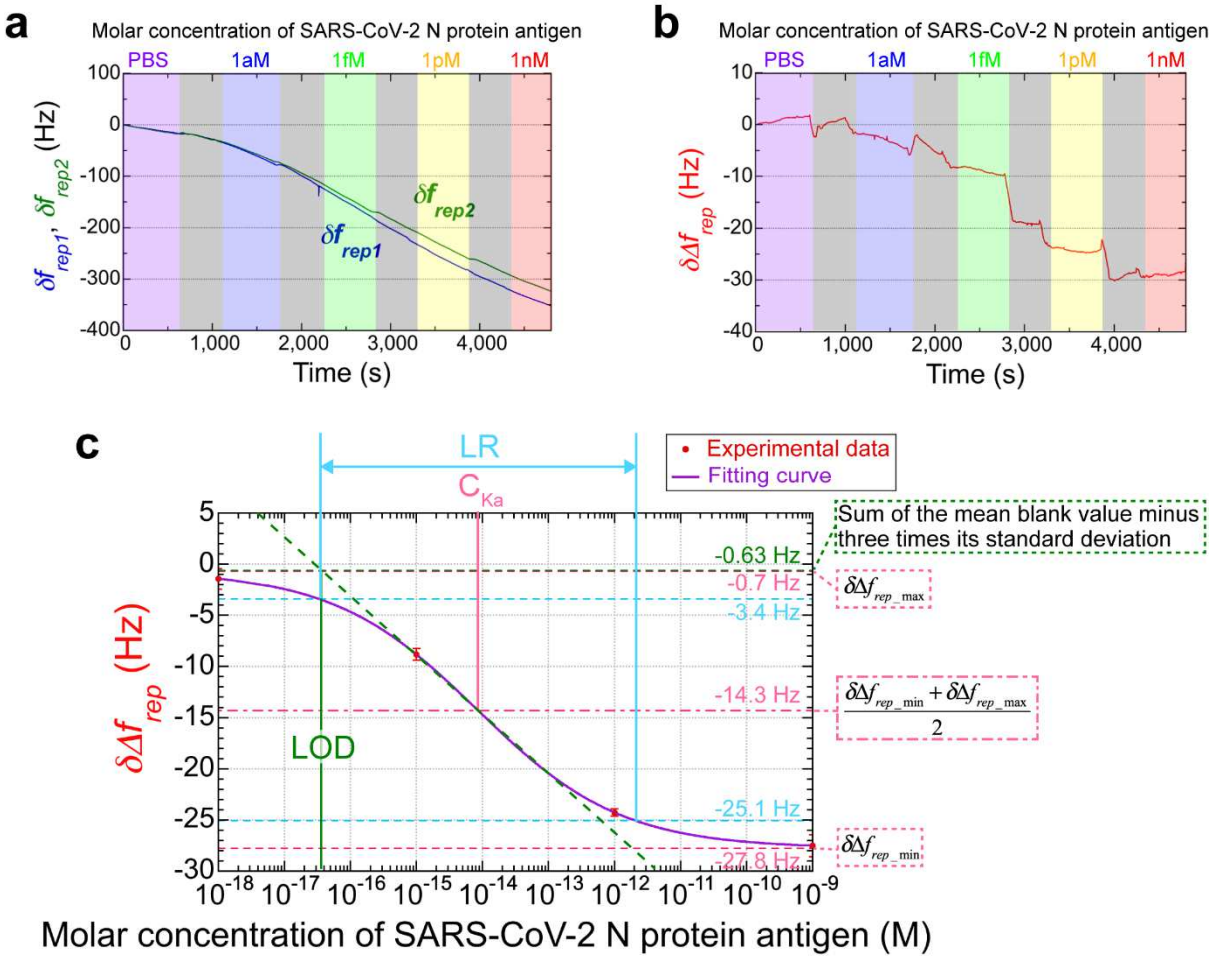

Fig. 3.7. Rapid, high-sensitivity, dual-comb biosensing of the SARS-CoV-2 N protein antigen. (a) Sensorgram of δf_{rep1} and δf_{rep2} with respect to different molar concentrations of the SARS-CoV-2 N protein antigen. δf_{rep1} and δf_{rep2} were calculated as the frequency deviations from the initial values of f_{rep1} and f_{rep2}, which were measured for the active biosensing OFC with immobilized antibody and the dummy OFC without immobilized antibody, respectively [see Table 3.1 and Fig. 3(d)]. Grey zones indicate the time period for sample exchange. (b) Sensorgram of $\delta\Delta f_{rep}$ with respect to different molar concentrations of the SARS-CoV-2 N protein antigen. $\delta\Delta f_{rep}$ was calculated as the frequency deviation from the initial value of Δf_{rep}. (c) Relationship between the antigen molar concentration and $\delta\Delta f_{rep}$. Red circles show experimental data obtained from the sensorgram of $\delta\Delta f_{rep}$. The purple line shows the fitting curve for the sigmoidal function of the Hill plot.

3.3 Discussion

To achieve the rapid, high-sensitivity detection of biomolecules, we developed dual-comb biosensing. Benefiting from the photonic-to-RF conversion in OFC, the enhanced sensitivity by the intracavity biosensor, and the active-dummy dual-comb compensation of temperature drift, the detection of the SARS-CoV-2 N protein antigen with a molar concentration from1 aM to 1nM was demonstrated in the measurement time of 10 min.

We first perform the quantitative analysis of the result shown in Fig. 3.7(c). The antigen-antibody reaction is represented by a sigmoidal curve, often used when discussing the biosensor performance [62]; thus, the sigmoidal curve was applied to the experimental data to evaluate the ability of dual-comb biosensing to sense the SARS-CoV-2 N protein antigen. The sigmoidal function of Hill plot is given by

$$\delta\Delta f_{rep} = \delta\Delta f_{rep\_\min} + \frac{\delta\Delta f_{rep\_\max} - \delta\Delta f_{rep\_\min}}{1+\left(\frac{[C]}{[C_{Ka}]}\right)^{n}}, \qquad (2)$$

where $\delta\Delta f_{rep\_max}$ and $\delta\Delta f_{rep\_min}$ are the maximum and minimum of $\delta\Delta f_{rep}$ within a range of 1 aM to 1 nM, n is the Hill coefficient, C is the concentration of the antigen, and C_{Ka} is the dissociation constant. The purple line in Fig. 3.7(c) represents the sigmoidal fit of the experimental data. Unfortunately, in this fitting analysis, as the number of unknown parameters of the sigmoidal curve (N = 4, $\delta\Delta f_{rep\_min}$, $\delta\Delta f_{rep\_max}$, C_{Ka}, and n) is equal to the number of input data (N = 4, concentrations of 1 aM, 1 fM, 1 pM, and 1 nM), the degrees of freedom for the fitting are zero. In other words, results of this fit may be unreliable. The primary focus here is to roughly calculate performance parameters for biosensing using experimental data within specific concentration

ranges. Based on the zero-degree-of-freedom fitting results, we will then proceed to engage in the following discussions. Addressing the issue of the zero-degree-of-freedom fitting results through detailed quantitative analysis will be part of our future work. From the curve fitting analysis of experimental plots with Eq. 2, we determined the following four parameters: $\delta\Delta f_{rep\_min}$ = -27.8 Hz, $\delta\Delta f_{rep\_max}$ = -0.7 Hz, C_{Ka} = 8.4 fM, and n = 0.40. C_{Ka} [see the pink solid line in Fig. 3.7(c)] is corresponding to the molar concentration at the middle [= -14.3 Hz, see pink the dashdotted line in Fig. 3.7(c)] between $\delta\Delta f_{rep\_max}$ and $\delta\Delta f_{rep\_min}$ [see pink dashed lines in Fig. 3.7(c)]. When the linear range (LR) was defined as the molar concentration at 10 ~ 90 % (= -3.4 ~ -25.1 Hz) of the dynamic signal range of $\delta\Delta f_{rep\_max}$ to $\delta\Delta f_{rep\_min}$ [see blue dashed lines in Fig. 3.7(c)] [43], it was determined to be 34 aM ~ 2.1 pM [see blue solid lines in Fig. 3.7(c)]. Since the mean $\delta\Delta f_{rep}$ value (= 0.93 Hz) minus three times its standard deviation (= 0.52 Hz) of the blank sample (PBS) was -0.63 [see the purple zone in Fig. 3.7(b)], the LOD was calculated to be 37 aM from the crossover point [see the green solid line in Fig. 3.7(c)] between it and the linear approximation given by the Hill coefficient n (= 0.40).

We next compare the performance between the dual-comb biosensing and other biosensors when they are applied for biosensing of SARS-CoV-2 protein. While SPR benefits from the rapid analysis, its analytical sensitivity remains in LR of 2 ~ 1000 ng/mL with LOD of 1.02 pM [63]. The plasmonic enhancement by large gold nanoparticle decreases the LOD of SPR down to 85 fM or 4 pg/ml [49]. Also, the dual-functional plasmonic biosensor combining the plasmonic photothermal effect and localized SPR indicates LOD of 0.22 pM and LR of 0.1 pM ~ 1 μM [64]. In addition to these optical biosensors, colorimetric assay can be used for the detection of SARS-CoV-2 with a LOD of 0.18 ng/μL and a LR of 0.2 ~ 3 ng/μL within 10 min [65]. Dual-comb biosensing of SARS-CoV-2 N protein antigen achieves a LOD of 37 aM and a LR of 34 aM ~ 2.1 pM within 10 min in a simple matrix of PBS buffer that contains no interfering proteins, enzymes, and biomolecules. The above LOD and LR given in molar concentration correspond to concentrations of 1.7 fg/mL and 1.6 fg/mL ~ 99 pg/mL based on the molecular weight of the SARS-CoV-2 N protein antigen (= 47 kDa). When using complex matrices such as blood plasma or serum in place of PBS, testing time may increase depending on analyte diffusion and/or binding kinetics; still, it's within a range of 10 minute. Table 3.2 summarizes the comparison of those biosensors for SARS-CoV-2 protein. In this way, the dual-comb biosensing greatly outperforms other biosensors in terms of LOD and LR.

Table 3.2. Comparison of testing methods for SARS-CoV-2

Method	Limit of detection	Linear range	Time	Matrix	Target
SPR	1.02 pM	2 ~ 1000 ng/mL	-	PBS containing 0.1 % Tween 20	N protein antigen
Nanoplasmonic-enhanced SPR	85 fM (4 pg/ml)	85 fM ~ 2 pM	5 min	PBS	N protein antigen
Dual-functional plasmonic biosensor	0.22 pM	0.1 pM ~ 1 μM	-	Nuclease-free water	Nucleic acid
Colorimetric assay	0.18 ng/μL	0.2 ~ 3 ng/μL	10 min	RNase H reaction buffer	N phosphoprotein gene
Dual-comb biosensing	37 aM (1.7 fg/ml)	34 aM ~ 2.1 pM (1.6 fg/ml ~ 99 pg/ml)	10 min	PBS	N protein antigen

Since we demonstrated the dual-comb biosensing of SARS-CoV-2 N protein antigen using highly purified, synthetic laboratory samples, the demonstrated results could not guarantee about the real specificity in the detection, which is another important performance of biosensing. For a real assessment of the biosensing performance including the specificity, a sample of complex matrices such as blood plasma or serum should be evaluated. In this case, non-specific adsorption of other proteins on the sensor surface spoils the specificity of dual-comb biosensing. We have to make special surface modifications designed to avoid non-specific adsorption in the active and the dummy sensing OFCs together with a specific antibody of SARS-CoV-2 N protein enhancing the specificity. Use of nucleic acids (DNA probe), in place of antibody-antigen, as biomolecular interaction also enables us to enhance the specificity of dual-comb biosensing largely. Work is in progress to enhance the specificity of the dual-comb biosensing by these approaches.

We finally discuss the potential for dual-comb biosensing to be used for the detection of other biomolecules of interest. The achieved C_{Ka} (= 8.4 fM) is considerably low, enabling its easy use for a wide variety of biosensing applications. For example, it has an option for early detection and quantification of cancer cells from a droplet of blood or other body fluids by

detecting a sugar chain specifically expressed on the surface of cancer cells. Such liquid biopsy will be a powerful tool for detection of important biomarkers, such as proteins or RNA, in addition to cancer cells. Furthermore, if the molecular identification in biosensing is implemented by DNA probes in place of antigen-antibody reactions, it enables biosensing of exosomes via miRNA. As exosomes play an important role for intercellular communication, the biosensing of them is expected to make a great contribution to the diagnosis (marker) and treatment (drug delivery) of diseases such as cancer and Alzheimer's disease.

3.4 Materials and Methods

3.4.1 General principle of operation

Figure 3.1(b) shows a schematic diagram of the intracavity MMI fiber sensor with antibody surface modification. When the surface of the fiber sensor is not modified with an antibody, the MMI fiber sensor functions as an RI sensor. The MMI fiber sensor is composed of a clad-less multimode fiber (MMF; Thorlabs Inc., Newton, NJ, USA, FG125LA, core diameter= 125 μm, fiber length = 58.94 mm) with a pair of single-mode fibers (SMFs) at both ends (Corning Inc., Corning, NY, USA, SMF28e+, core diameter = 8.2 μm, cladding diameter=125 μm, fiber length = 150 mm). Only the exposed core of the clad-less MMF functions as a sensing part. The OFC light passing through the input SMF is diffracted at the entrance face of the clad-less MMF and then undergoes repeated total internal reflection at the boundary between the clad-less MMF core surface and the sample solution. Only the OFC modes satisfying the MMI wavelength λ_{MMI} can exit through the clad-less MMF and then be transmitted through the output SMF. λ_{MMI} is given by

$$\lambda_{MMI} = \frac{n_{MMF} m_{MMI}}{L_{MMF}} \left[D\left(n_{sam}\right) \right]^2, \qquad (3)$$

where L_{MMF} and n_{MMF} are the geometrical length and RI of the clad-less MMF, m_{MMI} is the order of the MMI, n_{sam} is the RI near the clad-less MMF core surface (namely, sample RI), and $D(n_{sam})$ is the effective core diameter of the clad-less MMF. Since $D(n_{sam})$ is influenced by the Goos-Hänchen shift on the core surface of the clad-less MMF, λ_{MMI} is a function of the sample RI near the sensor surface. The intracavity MMI fiber sensor in this study functions as an RI-dependent optical bandpass filter tunable around λ_{MMI} (= 1556.6 nm) with constructive interference at m = 4. This λ_{MMI} was selected to match a spectral peak of the fiber OFC, suppressing the power loss. The RI-dependent λ_{MMI} shift of the OFC is converted into an RI-dependent f_{rep} shift via the wavelength dispersion of the cavity fiber [see Fig. 3.1(a)]. Furthermore, if the surface of the MMI fiber sensor is modified with a virus antibody, then the RI-dependent f_{rep} shift is converted into a

virus-antigen-concentration-dependent f_{rep} shift through antibody-antigen reactions. In other words, the intracavity MMI fiber sensor with antibody surface modification enables a photonic RF biosensor for viruses.

3.4.2 Single-comb configuration of the sensing OFC

We used a linear fiber cavity mode-locked by a saturable absorber mirror for easy, stable, mode-locked oscillation and compact size [see Fig. 3.2(a)]. The linear cavity includes a 2.6-m-long SMF (SMF; Corning Inc., Corning, NY, USA, SMF28e+, dispersion at 1550 nm = 17 ps•km^{-1}•nm^{-1}), a 0.6-m-long erbium-doped fiber (EDF; nLIGHT Inc., Camas, WA, USA, LIEKKI ER30-4/125, dispersion at 1550 nm = -22.75 ps•km^{-1}•nm^{-1}), a saturable absorber mirror (BATOP GmbH, Jena, Germany, SAM-1550-55-2ps-1.3b-0, high reflection band = 1480-1640 nm, absorbance = 55 %, modulation depth = 2.4 %, relaxation time constant = ~2 ps, size = 1.3 mm width, 1.3 mm height, 0.4 mm thickness), a wavelength-division-multiplexing coupler (WDM; AFR Ltd., Zhuhai, China, WDM-1-9855-N-B-1-F), a pumping laser diode (LD pump source; Thorlabs Inc., Newton, NJ, USA, BL976-PAG700, wavelength = 976 nm, power = 700 mW), a 90:10 fiber output coupler (OC; AFR Ltd., Zhuhai, China, PMOFM-55-2-B-Q-F-90), and an intracavity MMI fiber sensor (MMI). The total dispersion of the fiber cavity was set to -0.12 pm/s^2 for stable operation. The fiber cavity was placed in an aluminum box, and its temperature was not actively controlled. The light output of the sensing OFC was detected by a photodetector (PD; Thorlabs Inc., Newton, NJ, USA, PDA05CF2, wavelength = 800~1700 nm, frequency bandwidth = 150 MHz), and the resulting frequency signal of f_{rep} was measured by an RF frequency counter (Keysight Technologies, Santa Rosa, CA, USA, 53230A, frequency resolution = 12 digit•s^{-1}) synchronized to a rubidium frequency standard (Stanford Research Systems Inc., Sunnyvale, CA, USA, FS725, frequency = 10 MHz, accuracy = 5×10^{-1}, and instability = 2×10^{-11} at 1 s).

3.4.3 Dual-comb configuration of active and dummy sensing OFCs

We used a pair of linear-cavity sensing OFCs (frequency spacing = f_{rep1} and f_{rep2}, frequency difference between them = $\Delta f_{rep} = f_{rep1} - f_{rep2}$) for the active sensing OFC and the dummy sensing OFC in the dual-comb configuration [see Fig. 3.3(a)]. The configuration of each linear cavity was similar to that in Fig. 3.2(a). The output light of the LD pump source was split into two beams and used for these two OFCs, which eliminates the influence of power drifts in the LD pump source through common-mode behavior. These OFC fiber cavities were enclosed in an aluminum box. Specification of the active and dummy sensing OFCs are shown in Table 3.1. The light output of the dual OFCs was detected by a pair of PDs, and the resulting frequency signals of f_{rep1}, f_{rep2} and Δf_{rep} were measured through a combination of an RF frequency counter and a rubidium frequency standard.

3.4.4 Recombinant SARS-CoV-2 nucleocapsid protein antigen

The recombinant SARS-CoV-2 nucleocapsid protein, expressed in Escherichia coli, was used as an antigen. The molecular weight of 47 kDa was calculated based on the amino acid sequence of 419 residues using the molecular weight calculation tool provided by Expasy. We further validated this by referring to literature that documented the utilization of a similar N capsid protein. The slight variation in molecular weight compared to previous literature is thought to be attributed to differences in the His-Tag sequence and/or uncertainties in band reading on SDS-PAGE.

3.4.5 Enzyme-linked immunosorbent assay (ELISA)

Recombinant SARS-CoV-2 nucleocapsid protein antigen (FPZ0513, 2 μg/ml) in phosphate-buffered saline (PBS) was added to 96-well EIA/RIA plates (Corning Inc., Corning, NY, U.S.) and incubated overnight at room temperature. Non-specific sites were blocked with Blocking One (Nacalai Tesque, Inc., Kyoto, Japan). The plates were washed and diluted anti-SARS-CoV-2 nucleocapsid monoclonal antibody (FPZ0553) was added. After 1 hour incubation at room temperature and washing the plates, goat anti-mouse IgG, (H+L) horseradish peroxidase conjugated (Invitrogen) was used as the secondary antibody. After washing the plates two times, TMB substrate solution (Invitrogen, Thermo Fisher Scientific Inc., Waltham, MA, U.S.) was added. The OD at 450 nm for each well was measured using a SpectraMax ABS microplate reader (Molecular Devices, San Jose, CA, U.S.).

3.4.6 Antibody modification of the MMI fiber sensor

A schematic diagram of the intracavity MMI fiber sensor with antibody surface modification is shown in Fig. 3.1(b). First, a UV ozone cleaner (Sun Energy Corp., Minoo, Osaka, Japan, SKB1101N-01) was applied to the MMI fiber sensor for 30 min to remove any organic compounds on the surface of the clad-less MMF and modify the resulting surface with hydroxy groups. Second, the surface of the clad-less MMF was modified with amino-terminated groups through a silane coupling reaction using 1 % (v/v) 3-aminopropyltriethoxysilane (APTES) in ethanol for 1 hour, followed by washing with ultrapure water and drying at 110 °C for 10 min. Third, for the antibody immobilization step by amide bonding, a dehydro-condensation reaction was used, which is a one-step reaction with higher reaction efficiency even in buffer solution, instead of the conventional method using carbodiimide activation [60]. The monoclonal antibody specific for the N protein antigen was immobilized on the amino-group-coated MMF core by a dehydration-condensation reaction using 10 mM 4-(4,6-dimethoxy-1,3,5-triazin-2-yl)-4-methylmorpholinium chloride (DMTMM) in PBS buffer (pH 7.4) [61].

3.4.7 Data analysis

The frequency spacings of the OFCs (f_{rep}, f_{rep1}, and f_{rep2}) were continuously acquired by an RF frequency counter with a gate time of 100 ms and a sampling interval of 2.8 s. The

frequency difference Δf_{rep} between f_{rep1} and f_{rep2} was calculated from acquired f_{rep1} and f_{rep2}. Finally, δf_{rep}, δf_{rep1}, δf_{rep2}, and $\delta \Delta f_{rep}$ were calculated as the frequency deviations from the initial values of f_{rep}, f_{rep1}, f_{rep2}, and Δf_{rep}, respectively. In the dual-comb biosensing of SARS-CoV-2 N protein antigen, we calculated the 99.9 % confidence interval for the first 100 data of the $\delta \Delta f_{rep}$ sensorgram measured in the PBS, and then used it as a criterion of rejection test to judge whether $\delta \Delta f_{rep}$ value acquired at each molar concentration is considered as a measurement error.

4. Conclusion

This doctoral dissertation investigates two main themes to enhance the sensing performance to a level suitable for deployment in biosensing applications by addressing the temperature drift issue in RI-sensing using MMI fiber sensors and fiber OFC.

(1) Reduction of temperature drift in refractive-index-sensing optical frequency comb by active-dummy compensation of dual-comb configuration [78]

(2) Rapid, high-sensitivity detection of biomolecules using dual-comb biosensing [79]

In the first theme, we developed a temperature-compensated RI-sensing OFC (dual-comb RI-sensing) by applying the active-dummy compensation method commonly used in strain measurements. This was achieved by using an active-sensing OFC sensitive to both temperature and refractive index, and a dummy-sensing OFC sensitive only to temperature, extracting the difference frequency signal of their repetition frequencies. To evaluate the temperature compensation performance of dual-comb RI-sensing, we investigated the effect of temperature drift on the difference in cavity lengths between the active-sensing and dummy-sensing OFCs. From the perspective of temperature compensation performance and RI measurement performance, we validated the appropriate difference in cavity lengths (Δf_{rep}) between the active-sensing and dummy-sensing OFCs. Concerning the temperature compensation performance for the difference in resonator lengths, the active-dummy temperature compensation did not function effectively when the difference in resonator lengths was about 100mm (equivalent to 1000 kHz in Δf_{rep}), but a significant effect of temperature compensation performance was observed when the difference in cavity lengths was about 10mm (equivalent to 110 kHz in Δf_{rep}) or less, with better temperature compensation performance observed for smaller differences in cavity lengths. Therefore, considering the precision of fiber OFC cavity fabrication, it is desirable to select a difference in cavity lengths of about 10mm or less (equivalent to 110 kHz or less in Δf_{rep}). However, several factors remain to be considered for further improvement in temperature compensation performance. Firstly, achieving a resonator length difference (Δf_{rep}) of zero due to the precision of resonator length fabrication is difficult, and Δf_{rep} is limited to a few kHz. Although it is possible to fine-tune the resonator length difference by inserting delay lines using free-space optical systems, this may compromise mechanical stability, leading to a potential decrease in the effectiveness of active-dummy temperature compensation. Secondly, to achieve precise active-dummy compensation, it is necessary to place the active and dummy combs in exactly the same location to ensure they experience exactly the same temperature effects. However, due to spatial constraints within the enclosure, there are limitations to this approach. Thirdly, for precise RI measurement, it is desirable for the optical spectra propagated by the active and dummy OFCs to

match completely. However, achieving perfect spectral alignment is challenging due to variations in the optical spectra within the cavity caused by the fabrication precision of MMI fiber sensors when using two independent MMI fiber sensors. To address these three factors, it is desirable to realize dual-comb within a single resonator and perform active-dummy compensation. Single-resonator dual-comb fiber lasers have recently attracted attention. Currently, integrating MMI fiber sensors into this laser is challenging. However, this configuration can simplify the measurement system and significantly improve the performance of dual-comb RI-sensing.

In the second theme, we extended dual-comb RI-sensing to biosensing by surface modification of SARS-CoV-2/NP antibody on the surface of MMI fiber sensor. By effectively reducing the temperature drift with an active-dummy temperature compensation method, the N protein antigen of SARS-CoV-2 was successfully sensed rapidly and accurately. Quantitative analysis of the sensing performance showed that the linear range (LR) was 34 aM ~2.1 pM and the limit of detection (LOD) was 38 aM. Comparison of performance with other SARS-CoV-2 assays showed that dual optical comb biosensing can detect SARS-CoV-2/NP antigens with a much shorter detection time than RT-PCR and an LOD approaching that of RT-PCR. Further improvement of temperature compensation is required for future development. The remaining temperature drift ($\delta \Delta f_{rep}$ = several Hz) after temperature compensation limits the LOD to 38 aM for the detection of SARS-CoV-2 N protein antigen. Since the frequency counter synchronized to the frequency standard is within an error of the order of 10^{-3} Hz, further suppression of the residual drift may reduce the LOD.

This PhD thesis highlighted the improvement of the performance of RI-sensing OFC and their application to biosensors. A temperature compensation method was developed to reduce the drift of the sensor signal due to temperature fluctuation, which is a problem of RI-sensing combs. The improved accuracy of the sensing by the temperature compensation method enables its deployment in biosensors, and the N-protein antigen of SARS-CoV-2 was detected rapidly and with high accuracy. This method is expected to detect not only new coronaviruses but also various infectious disease viruses. In the future, we expect that rapid and highly accurate detection of viruses in the event of a pandemic will contribute to the prevention of the spread of infection and early treatment. Furthermore, ensing OFC is expected to be applied to biomarkers. Recently, personalized medicine has been gaining popularity as a new form of healthcare. Personalized medicine is an approach that considers individual factors such as genetics, environment, and lifestyle to provide optimal medical strategies and treatments, allowing for more effective and safer treatments and preventive care. By utilizing biomarkers, it is possible not only to select the most suitable treatment for individuals but also to identify the risk of disease onset early and take preventive measures. In the future, if sensing OFC can be applied to biomarkers, it is

expected to contribute to extending healthy life expectancy and reducing medical expenses through preventive healthcare, which involves high-precision early diagnosis of diseases and consideration of preventive measures. Modern society faces various challenges such as aging, increasing chronic diseases, extending healthy life expectancy, and preventing infections by new viruses. However, sensing OFC is considered to be an effective tool for addressing these challenges.

References

[1] S. Singh, “Refractive index measurement and its applications,”Phys. Scr. 65, 167-180(2002).

[2] H. Suzuki, M. Sugimoto, Y. Matsui, and J. Kondo,“Effects of gold film thickness on spectrum profile and sensitivity of a multimode-optical-fiber SPR sensor,” Sens. Actuator B-Chem. 132, 26–33 (2008).

[3] S. K. Chauhan, N. Punjabi, D. K. Sharma, and S. Mukherji, “A silicon nitride coated LSPR based fiber-optic probe for possible continuous monitoring of sucrose content in fruit juices,” Sens. Actuator B-Chem. 222, 1240–1250 (2016).

[4] B. Sutapun, M. Tabib-Azar, and A. Kazemi, “Pd-coated elastooptic fiber optic Bragg grating sensors for multiplexed hydrogen sensing,” Sens. Actuator B-Chem. 60, 27–34 (1999).

[5] J. R. Ott, M. Heuck, C. Agger, P. D. Rasmussen, and O. Bang, “Label-free and selective nonlinear fiber-optical biosensing,” Opt. Express. 16, 20834–20847 (2008).

[6] D. Monzón-Hernández and J. Villatoro, “High-resolution refractive index sensing by means of a multiple-peak surface plasmon resonance optical fiber sensor,” Sens. Actuator B-Chem. 115, 227–231 (2006).

[7] X. Shi, S. Zheng, H. Chi, X. Chi, X. Jin, and X. Zhang, “Refractive index sensor based on tilted fiber Bragg grating and stimulated Brillouin scattering”Opt. Express. 20, 10853-10858 (2012).

[8] H. Fukano, T. Aiga, and S. Taue, “High-sensitivity fiber-optic refractive index sensor based on multimode interference using small-core single-mode fiber for biosensing,” Jpn. J. Appl. Phys. 53, 04EL08 (2014).

[9] S. Liu, Z. Yin, L. Zhang, L. Gao, X. Chen, and J. Cheng, “Multilongitudinal mode fiber laser for strain measurement,” Opt. Lett. 35, 835-837 (2010).

[10] T. Guo, A. C. Wong, W. S. Liu, B. O. Guan, C. Lu, and H. Y. Tam, “Beat-frequency adjustable Er3+-doped DBR fiber laser for ultrasound detection,” Opt. Express. 19, 2485-2492 (2011).

[11] Y. Liang, L. Jin, L. Wang, X. Bai, L. Cheng, and B.-O. Guan, “Fiber-Laser-Based Ultrasound Sensor for Photoacoustic Imaging,” Sci. Rep. 7, 40849 (2017).

[12] T. Udem, J. Reichert, R. Holzwarth, and T. W. Hänsch, “Accurate measurement of large optical frequency differences with a mode-locked laser,” Opt. Lett. 24, 881–883 (1999).

[13] M. Niering, R. Holzwarth, J. Reichert, P. Pokasov, T. Udem, M. Weitz, T. W. Hänsch, P.Lemonde, G. Santarelli, M. Abgrall, P. Laurent, C. Salomon, and A. Clairon, “Measurement of the hydrogen 1S- 2S transition frequency by phase coherent comparison with a microwave cesium fountain clock,” Phys. Rev. Lett. 84, 5496–5499 (2000).

[14] T. Udem, R. Holzwarth, and T. W. Hänsch, “Optical frequency metrology,” Nature 416, 233–237 (2002).

[15] S. A. Diddams, L. Hollberg, and V. Mbele, "Molecular fingerprinting with the resolved modes of a femtosecond laser frequency comb," Nature 445, 627–630 (2007).

[16] T. Minamikawa, Y.-D. Hsieh, K. Shibuya, E. Hase, Y. Kaneoka, S. Okubo, H. Inaba, Y. Mizutani, H. Yamamoto, T. Iwata, and T. Yasui, "Dual-comb spectroscopic ellipsometry," Nat. Commun. 8, 610 (2017).

[17] N. Kuse, A. Ozawa, and Y. Kobayashi, "Static FBG strain sensor with high resolution and large dynamic range by dual-comb spectroscopy," Opt. Express. 21, 11141–11149 (2013).

[18] I. Coddington, W. C. Swann, L. Nenadovic, and N. R. Newbury, "Rapid and precise absolute distance measurements at long range," Nat. Photonics. 3, 351–356 (2009).

[19] K. Minoshima and H. Matsumoto, "High-accuracy measurement of 240-m distance in an optical tunnel by use of a compact femtosecond laser," Appl. Opt. 39, 5512–5517 (2000).

[20] K. Minoshima, K. Arai, and H. Inaba, "High-accuracy self-correction of refractive index of air using two-color interferometry of optical frequency combs," Opt. Express. 19, 26095–26105 (2011).

[21] G. Wu, M. Takahashi, K. Arai, H. Inaba, and K. Minoshima, "Extremely high-accuracy correction of air refractive index using two-colour optical frequency combs," Sci. Rep. 3, 1894 (2013).

[22] T. Minamikawa, T. Ogura, Y. Nakajima, E. Hase, Y. Mizutani, H. Yamamoto, K.Minoshima, and T. Yasui, "Strain sensing based on strain to radio-frequency conversion of optical frequency comb," Opt. Express. 26, 9484-9491 (2018).

[23] S. Wang, P. Lu, H. Liao, L. Zhang, D. Liu, and J. Zhang, "Passively mode-locked fiber laser sensor for acoustic pressure sensing," J. Mod. Opt. 60,1892-1897 (2013).

[24] T. Minamikawa, T. Masuoka, T. Ogura, K. Shibuya, R. Oe, E. Hase, Y. Nakajima, Y.Yamaoka, T. Mizuno, M. Yamagiwa, Y. Mizutani, H. Yamamoto, T. Iwata, K.Minoshima, and T. Yasui, "Ultrasonic wave sensing using optical-frequency-comb sensing cavity for photoacoustic imaging," OSA Continuum. 2, 439-449 (2019).

[25] Y. Jung, S. Kim, D. Lee, and K. Oh, "Compact three segmented multimode fibre modal interferometer for high sensitivity refractive-index measurement," Meas. Sci. Technol. 17,1129–1133 (2006).

[26] Q. Wang and G. Farrell, "All-fiber multimode-interference-based refractometer sensor: proposal and design," Opt. Lett. 31, 317–319 (2006).

[27] S. Taue, Y. Matsumoto, H. Fukano, and K. Tsuruta, "Experimental analysis of optical fiber multimode interference structure and its application to refractive index measurement,"Jpn. J. Appl. Phys. 51, 04DG14 (2012).

[28] R. Oe, S. Taue, T. Minamikawa, K. Nagai, K. Shibuya, T. Mizuno, M. Yamagiwa, Y. Mizutani, H. Yamamoto, T. Iwata, H. Fukano, Y. Nakajima, K. Minoshima, and T. Yasui, "Refractive-index-

sensing optical comb based on photonic radio-frequency conversion with intracavity multi-mode interference fiber sensor," Opt. Express. 26, 19694-19706 (2018)

[29] R. Oe, T. Minamikawa, S. Taue, H. Koresawa, T. Mizuno, M. Yamagiwa, Y. Mizutani, H.Yamamoto, T. Iwata, and T. Yasui, "Refractive index sensing with temperature compensation by a multimode-interference fiber-based optical frequency comb sensing cavity," Opt. Express. 27, 21463-21476 (2019).

[30] R. Oe, T. Minamikawa, S. Taue, T. Nakahara, H. Koresawa, T. Mizuno, M. Yamagiwa, Y. Mizutani, H. Yamamoto, T. Iwata, Y. Nakajima, K Minoshima, T. Yasui, "Improvement of dynamic range and repeatability in a refractive-index-sensing optical comb by combining saturable-absorber-mirror mode-locking with an intracavity multimode interference fiber sensor," Jpn. J. App. Phys. 58, 060912 (2019).

[31] Y. Nakajima, Y. Kusumi, and K. Minoshima, "Mechanical sharing dualcomb fiber laser based on an all-polarization-maintaining cavity configuration," Opt. Lett. 46, 5401-5404 (2016).

[32] T. Yumoto, W. Kokuyama, S. Matsubara, T.i Yasui, and Y. Nakajima, "All-polarization-maintaining dual-comb fiber laser with mechanically shared cavity configuration and micro-optic component," Opt. Continuum, 2, 1867-1874 (2023).

[33] X. Zhao, T. Li, Y. Liu, Q. Li, Z. Zheng, "Polarization-multiplexed, dual-comb all-fiber mode-locked laser," Photonics. Res. 6, 853-857 (2018).

[34] X. Zhao, G. Hu, B. Zhao, C. Li, Y. Pan, Y. Liu, T. Yasui, Z. Zheng, "Picometer-resolution dual-comb spectroscopy with a free-running fiber laser," Opt. Express. 24, 21833-21845 (2016).

[35] Y. Nakajima, Y. Hata, and K. Minoshima, "High-coherence ultrabroadband bidirectional dual-comb fiber laser," Opt. Express. 27, 5931-5944 (2019).

[36] T. Suo, X. Liu, J. Feng, M. Guo, W. Hu, D. Guo, H. Ullah, Y. Yang, Q. Zhang, X. Wang, M. Sajid, Z. Huang, L. Deng, T. Chen, F. Liu, K. Xu, Y. Liu, Q. Zhang, Y. Liu, Y. Xiong, G. Chen, K. Lan, Y. Chen, "ddPCR: a more accurate tool for SARS-CoV-2 detection in low viral load specimens," Emerg. Microbes & infec. 9, 1259-1268 (2020).

[37] N. Panpradist, W. Qin, P. S. Ruth, J. H. Kotnik, A. K. Oreskovic, A. Miller, S. W. A. Stewart, J. Vrana, P. D. Hang, I. A. Beck, L. M.Starita, L. M. Frenkel, B. R. Lutz, "Simpler and faster Covid-19 testing: Strategies to streamline SARS-CoV-2 molecular assays," EBioMedicine. 64, 103236 (2021).

[38] A. Oranger, C. Manzari, M. Chiara, E. Notario, B. Fosso, A. Parisi, A. Bianco, M. Iacobellis, M. d'Avenia, A. M. D'Erchia, G. Pesole, "Accurate detection and quantification of SARS-CoV-2 genomic and subgenomic mRNAs by ddPCR and meta transcriptomics analysis," Commun. Biol. 4, 1215 (2021).

[39] S. M. Borisov, O. S. Wolfbeis, "Optical biosensors," Chem. Rev. 108, 423-461 (2008).

[40] P. Damborský, J. Švitel, J. Katrlík, "Optical biosensors," Essays Biochem. 60, 91-100 (2016).

[41] J. Homola, S. S. Yee, G. Gauglitz, "Surface plasmon resonance sensors," Sens. Actuators. B 54, 3–15 (1999).

[42] P. Pattnaik, "Surface plasmon resonance," Appl. Biochem. Biotechnol. 126, 079–092 (2005).

[43] Y. Liu, C. Z. Huang, "One-step conjugation chemistry of DNA with highly scattered silver nanoparticles for sandwich detection of DNA," Analyst. 137, 3434-3436 (2012).

[44] N. A. S. Omar, Y. W. Fen, J. Abdullah, A. R. Sadrolhosseini, Y. M. Kamil, N. I. M. Fauzi, H. S. Hashim, M. A. Mahdi, "Quantitative and selective surface plasmon resonance response based on a reduced graphene oxide-polyamidoamine nanocomposite for detection of dengue virus e-proteins," Nanomaterials. 10, 569 (2020).

[45] H. Ashiba, Y. Sugiyama, X. Wang, H. Shirato, K. Higo-Moriguchi, K. Taniguchi, Y. Ohki, M. Fujimaki, "Detection of norovirus virus-like particles using a surface plasmon resonance-assisted fluoroimmunosensor optimized for quantum dot fluorescent labels," Biosens. Bioelectron. 93, 260-266 (2017).

[46] H. Bai, R. Wang, B. Hargis, H. Lu, Y. Li, "A SPR aptasensor for detection of avian influenza virus H5N1," Sensors. 12, 12506-12518 (2012).

[47] A. Djaileb, B. Charron, M. H. Jodaylami, V. Thibault, J. Coutu, K. Stevenson, S. Forest, L. S. Live, D. Boudreau, J. N. Pelletier, J.-F. "Masson, A rapid and quantitative serum test for SARS-CoV-2 antibodies with portable surface plasmon resonance sensing," ChemRxiv (2020).

[48] M. Moznuzzaman, I. Khan, M. R. Islam, "Nano-layered surface plasmon resonance based highly sensitive biosensor for virus detection: A theoretical approach to detect SARS-CoV-2," AIP Adv. 11, 065023 (2021).

[49] T. Yano, T. Kajisa, M. Ono, Y. Miyasaka, Y. Hasegawa, A. Saito, K. Otsuka, A. Sakane, T. Sasaki, K. Yasutomo, R. Hamajima, Y. Kanai, T. Kobayashi, Y. Matsuura, M. Itonaga, T. Yasui, "Ultrasensitive detection of SARS-CoV-2 nucleocapsid protein using large gold nanoparticle-enhanced surface plasmon resonance," Sci. Rep. 12, 1-8 (2022).

[50] S. Bian, J. Lu, F. Delport, S. Vermeire, D. Spasic, J. Lammertyn, A. Gils,"Development and validation of an optical biosensor for rapid monitoring of adalimumab in serum of patients with Crohn's disease," Drug Test. Anal. 10, 592-596 (2018).

[51] M. Singh, M. Holzinger, M. Tabrizian, S. Winters, N. C. Berner, S. Cosnier, G. S. Duesberg, "Noncovalently functionalized monolayer graphene for sensitivity enhancement of surface plasmon resonance immunosensors," J. Am. Chem. Soc. 137, 2800-2803 (2015).

[52] J. Pollet, K. P. F. Janssen, K. Knez, J. Lammertyn, "Real-time monitoring of solid phase PCR using fiber-optic SPR," Small. 7, 1003–1006 (2011).

[53] D. Daems, K. Knez, F. Delport, D. Spasic, J. Lammertyn, "Real-time PCR melting analysis with

fiber optic SPR enables multiplex DNA identification of bacteria," Analyst. 141, 1906-1911 (2016).

[54] V. Malachovská, C. Ribaut, V. Voisin, M. Surin, P. Leclère, R. Wattiez, C. Caucheteur, "Fiber-optic SPR immunosensors tailored to target epithelial cells through membrane Receptors," Anal. Chem. 87, 5957-5965 (2015).

[55] P. Leonard, S. Hearty, J. Quinn, R. O'Kennedy, "A generic approach for the detection of whole Listeria monocytogenes cells in contaminated samples using surface plasmon resonance," Biosens. Bioelectron. 19, 1331-1335 (2004).

[56] C. R. Taitt, G. P. Anderson, F. S. Ligler, "Evanescent wave fluorescence biosensors: Advances of the last decade," Biosens. Bioelectron. 76, 103-112 (2016).

[57] M. J. Lochhead, K. Todorof, M. Delaney, J. T. Ives, C. Greef, K. Moll, K. Rowley, K. Vogel, C. Myatt, X.-Q. Zhang, C. Logan, C. Benson, S. Reed, R. T. Schooley, "Rapid multiplexed immunoassay for simultaneous serodiagnosis of HIV-1 and coinfections," J. Clin. Microbiol. 49, 3584-3590 (2011).

[58] U. S. Dinish, C. Y. Fu, K. S. Soh, R. Bhuvaneswari, A. Kumar, M. Olivo, "Highly sensitive SERS detection of cancer proteins in low sample volume using hollow core photonic crystal fiber," Biosens. Bioelectron. 33, 293-298(2012).

[59] S. K. Srivastava, A. Shalabney, I. Khalaila, C. Grüner, B. Rauschenbach, I. Abdulhalim, "SERS biosensor using metallic nano-sculptured thin films for the detection of endocrine disrupting compound biomarker vitellogenin," Small. 10, 3579-3587 (2014).

[60] M. Kunishima, C. Kawachi, J. Monta, K. Terao, F. Iwasaki, S. Tani, "4-(4, 6-dimethoxy- 1, 3, 5-triazin-2-yl)-4-methyl-morpholinium chloride: an efficient condensing agent leading to the formation of amides and esters," Tetrahedron. 55, 13159-13170 (1999).

[61] T. Kajisa, T. Yano, H. Koresawa, K. Otsuka, A. Sakane, T. Sasaki, K. Yasutomo, T. Yasui, "Highly sensitive detection of nucleocapsid protein from SARS-CoV-2 using a near-infrared surface plasmon resonance sensing system," Opt. Continuum. 1, 2336-2346 (2022).

[62] G. Gauglitz, "Analytical evaluation of sensor measurements," Anal. Bioanal. Chem. 410, 5-13 (2018).

[63] J.-H. Bong, T.-H. Kim, J. Jung, S. J. Lee, J. S. Sung, C. K. Lee, M.-J. Kang, H. O. Kim, J.-C. Pyun, "Pig Sera-derived Anti-SARS-CoV-2 antibodies in surface plasmon resonance biosensors". Biochip J. 14, 358-368 (2020).

[64] G. Qiu, Z. Gai, Y. Tao, J. Schmitt, G. A. Kullak-Ublick, J. Wang, "Dual-functional plasmonic photothermal biosensors for highly accurate severe acute respiratory syndrome coronavirus 2 detection," ACS Nano. 14, 5268-5277 (2020).

[65] P. Moitra, M. Alafeef, K. Dighe, M. B. Frieman, D. Pan, "Selective naked-eye detection of SARS-CoV-2 mediated by N gene targeted antisense oligonucleotide capped plasmonic nanoparticles,"

ACS Nano. 14, 7617-7627 (2020).

[66] T. Nakahara, R. Oe, T. Kajisa, S. Taue, T. Minamikawa, T. Yasui, “Application of refractive-index-sensing optical frequency comb for biosensing of antigen-antibody reaction,” in Technical Digest of Conference on Lasers and Electro-Optics (CLEO) 2021, STu2A.2 (2021).

[67] B. Lee,”Review of the present status of optical fiber sensors,”Opt. Fiber Technol. 9, 57-79 (2003).

[68] S. Yin, P. B. Ruffin, and F. T. S. Yu,"Fiber optic sensors"CRC press (2017).

[69] S. K. Srivastava, R. Verma, and B. D. Gupta,”Surface plasmon resonance based fiber optic sensor for the detection of low water content in ethanol,”Sens. Actuator B Chem. 153, 194-198 (2011).

[70] U. Tiwari, P. Kumar, V. Mishra, S. C. Jain, N. Singh, P. Kapur, and L. M.Bharadwaj, “Immobilization of enzyme on long period grating fibers for sensitive glucose detection, ”Biosens. Bioelectron. 33, 190-195 (2012).

[71] J. Pollet, F. Delport, K.P.F. Janssen, K. Jans, G. Maes, H. Pfeiffer, M.Wevers, and J. Lammertyn, “Fiber optic SPR biosensing of DNA hybridization and DNA–protein interactions” Biosens. Bioelectron. 25, 864-869 (2009).

[72] Y. Tian, W. Wang, N. Wu, X. Zou, and X. Wang, “Tapered optical fiber sensor for label-free detection of biomolecules,” Sensors. 11, 3780-3790 (2011).

[73] M. P. DeLisa, Z. Zhang, M. Shiloach, S. Pielevar, C. C. Davis, J. S. Sirkis, and W. E. Bentley, “Evanescent wave long-period fiber Bragg grating as an immobilized antibody biosensor,” Anal. Chem. 72, 2895-2900 (2000).

[74] Z. Tian, S. S.-H. Yam, and H. P. Loock, “Refractive index sensor based on an abrupt taper Michelson interferometer in a single-mode fiber,” Opt. Lett. 33, 1105-1107 (2008).

[75] G. Yin, S. Lou, and H. Zou, “Refractive index sensor with asymmetrical fiber Mach–Zehnder interferometer based on concatenating single-mode abrupt taper and core-offset section,” Opt. Laser Technol. 45, 294–300, (2013).

[76] L. Coelho, D. Viegas, J. L. Santos, and J.M.M.M. de Almeida, “Enhanced refractive index sensing characteristics of optical fibre long period grating coated with titanium dioxide thin films,” Sens. Actuators B Chem. 202, 929-934, (2014).

[77] R. Slavik, J. Homola J. Čtyroký, and E. Brynda, “Novel spectral fiber optic sensor based on surface plasmon resonance,” Sens. Actuators B Chem. 74, 106-111, (2001).

[78] S. Miyamura, M. Higaki, S. Taue, Y. Nakajima, Y. Tokizane, E. Hase, T. Minamikawa, and T. Yasui, "Reduction of temperature drift in refractive-index sensing optical frequency comb by active-dummy compensation of dual-comb configuration," Journal of Lightwave Technology, early access (2024).

[79] S. Miyamura, R. Oe, T. Nakahara, H. Koresawa, S. Okada, S. Taue, Y.Tokizane, T. Minamikawa, T. Yano, K. Otsuka, A. Sakane, T. Sasaki, K.Yasutomo, T. Kajisa, and T. Yasui, "Rapid, high-

sensitivity detection of biomolecules using dual-comb biosensing, "Sci. Rep. 13, iss. 1, 14541 (2023).

[80] D. J. Jones, S. A. Diddams, J. K. Ranka, A. Stentz, R. S. Windeler, J. L. Hall, and S. T. Cundiff, "Carrier-envelope phase control of femtosecond mode-locked lasers and direct optical frequency synthesis," Science 288, 635–639 (2000).

[81] Fukano, D. Watanabe, and S. Taue, "Sensitivity characteristics of multimode-interference optical-fiber temperature-sensor with solid cladding material," IEEE Sens. J. 16, 8921-8927 (2016).

[82] R. C. Kamikawachi, I. Abe, A. S. Paterno, H. J. Kalinowski, M. Muller, J. L. Pinto, J. and L. Fabris," Determination of thermo-optic coefficient in liquids with fiber Bragg grating refractometer," Opt. Commun. 281, 621-625 (2008).

[83] C. Trono, F. Baldini, M. Brenci, F. Chiavaioli, and M. Mugnaini, "Flow cell for strain- and temperature-compensated refractive index measurements by means of cascaded optical fibre long period and Bragg gratings," Meas. Sci. Technol. 22 075204 (2011).